Peter Schaaf (Ed.)

Materials for Energy and Power Engineering (Werkstoffe für die Energietechnik)

Werkstofftechnik Aktuell

Schriftenreihe aus dem Fakultätsübergreifenden Institut für Werkstofftechnik (IWT) an der TU Ilmenau
Herausgegeben von Univ.-Prof. Dr. rer. nat. Peter Schaaf und Univ.-Prof. Dr.-Ing. Edda Rädlein

Band 7

Die vorliegende Schriftenreihe "Werkstofftechnik Aktuell" berichtet über aktuelle Forschungsergebnisse aus dem Institut für Werkstofftechnik (IWT) der TU Ilmenau. Die ausgewählten Texte spiegeln die breit gefächerten materialwissenschaftlichen und werkstofftechnischen Themen, die am IWT bearbeitet werden, wieder. Für weitere Informationen und Rückfragen können Sie sich gerne an das Institut (www.tu-ilmenau.de/wt) wenden oder das Institut persönlich besuchen. Über Ihre Anregungen, konstruktive Kritik und Ihre Kontaktaufnahme würden wir uns sehr freuen. Das IWT steht wissenschaftlichen Zusammenarbeiten stets aufgeschlossen gegenüber.

“Materials for Energy and Power Engineering”

(Werkstoffe für die Energietechnik)

Ilmenau University of Technology
4 - 7 September 2012

Edited by
Peter Schaaf

Universitätsverlag Ilmenau
2012

Impressum

Bibliografische Information der Deutschen Nationalbibliothek
Die Deutsche Nationalbibliothek verzeichnet diese Publikation in der Deutschen Nationalbibliografie; detaillierte bibliografische Angaben sind im Internet über http://dnb.d-nb.de abrufbar.

Wir danken für die finanzielle Unterstützung des
VDI Bezirksverein Thüringen, AK Werkstofftechnik.

Technische Universität Ilmenau/Universitätsbibliothek
Universitätsverlag Ilmenau
Postfach 10 05 65
98684 Ilmenau
www.tu-ilmenau.de/universitaetsverlag

Herstellung und Auslieferung
Verlagshaus Monsenstein und Vannerdat OHG
Am Hawerkamp 31
48155 Münster
www.mv-verlag.de

ISSN 1868-6532 (print)
ISBN 978-3-86360-035-8 (print)
URN urn:nbn:de:gbv:ilm1-2012100158

Titelfoto:

Scanning Electron micrographs (with artificial colors) of porous materials, which are currently tested at Ilmenau University of Technology for new batteries with improved efficiency and capacity.

(Rasterelektronenmikroskopaufnahmen (mit künstlichen Farben) von porösen Materialien, die an der TU Ilmenau für neue Batterieentwicklungen mit höherer Effizienz und Kapazität getestet werden.)

Contents

Preface

"Materials for Energy and Power Systems"

Peter Schaaf

Ilmenau University of Technology, Department of Electrical Engineering and Information Technology, Institute of Materials Engineering and Institute of Micro- and Nanotechnologies, Gustav-Kirchhoff-Strasse 5, 98693 Ilmenau, Germany

Energy conversion, energy harvesting, enery transport, energy storage, and energy distribution are one of the most challenging tasks our industrial societies have to cope with. A sustainable, smart, safe and ressources saving energy supply is depending on the development of clever and functional materials. It is the responsibility of all materials scientists and interdisciplinary working researchers to contribute to this challenge. Only combined interdisciplinary efforts from experts in research and industry in these fields of energy and power systems can solve the tremendous tasks we are facing in science and technology. New and smart materials for energy and power systems are a prerequisite to maintain our industrials and welfare standards.

The conference and workshop brought together a multi-disciplinary group of internationally recognized researchers and scholars. Thus it represented an opportunity to make contacts for collaboration or commercial exploitation in materials for energy applications and will give you an excellent overview of recent developments in the areas of energy conversion, energy storage, transport and efficiency. In addition, smart grids, sensors and actuators are becoming more and more important also in the energy field.

These proceedings of the IWK 2012 held in September at TU Ilmenau collect some important results from the symposium and the related workshop of "Materials for Energy and Power Systems". Whereas the field of photovoltaics is one of its own, other fields related to energy are becoming more and more important.

The most challenging topics of our today's energy challenges cover:

- energy conversion, solar heat, fuel cells, thermoelectrics, energy harvesting, power electronics, water pyrolysis, energy efficiency
- energy storage, materials for batteries, supercaps, superconductors, hydrogen storage, heat storage and isolation,
- energy transport, energy distribution, electrical contacts, switches, safety

A clear indication of the increasing importance of materials for energy is given in the following Fig. 1. There the exponential increase in publications (from ISI Web of Science) clearly proves the importance of the materials for energy.

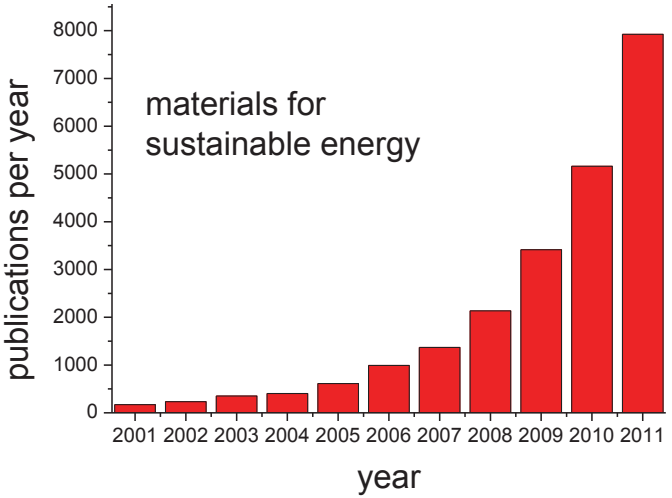

Figure 1: Number of publications related to "Materials for energy sustainability" per year as obtained from Web of Science (August 2012).

The most important materials are related to thermoelectrics [1], fuel cells [2], and heat storage [3]. Besides electrochemical energy storage [4], solar water slitting [5], superconductivity [6], materials for energy transport and distribution and energy harvesting are becoming more and more important [7].

References

[1] Snyder, G. Jeffrey; Toberer, Eric S. Complex thermoelectric materials. NATURE MATERIALS 2008, Volume: 7 Issue: 2 Pages: 105-114.

[2] Stambouli, AB; Traversa, E. Solid oxide fuel cells (SOFCs): a review of an environmentally clean and efficient source of energy. RENEWABLE & SUSTAINABLE ENERGY REVIEWS 2002, Volume: 6 Issue: 5 Pages: 433-455.

[3] Hasnain, SM. Review on sustainable thermal energy storage technologies, part I: Heat storage materials and techniques. ENERGY CONVERSION AND MANAGEMENT 1998, Volume: 39 Issue: 11 Pages: 1127-1138.

[4] Electrochemical energy storage to power the 21st century, MRS Bulletin, 2011, Volume 36, Issue 07.

[5] Recent developments in solar water-splitting photocatalysis, MRS Bulletin, 2011, Volume 36, Issue 01.

[6] Superconductivity at 100—Where we've been and where we're going, MRS Bulletin, Volume 36, Issue 08.

[7] Harnessing Materials for Energy, MRS Bulletin, 2008, Volume 33, Issue 4.

Entwicklung von Festkörperelektrolyten auf Basis von β”-Aluminiumoxidkeramiken für Na-Hochtemperaturbatterien

M. Grund, M. Schulz und U. Sydow

Fraunhofer-Institut für Keramische Technologien und Systeme (IKTS), Michael-Faraday-Str. 1, 07629 Hermsdorf

Abstract

Na-Beta-Aluminat Keramiken werden aufgrund ihrer guten Leitfähigkeit für Natriumionen und ihrer Stabilität als Festkörperelektrolyt in Na/$NiCl_2$- oder Na/S Akkumulatoren eingesetzt. Um eine hohe Ionenleitfähigkeit des Elektrolyten zu gewährleisten, werden die Akkumulatoren bei 270 - 350 °C betrieben. Die Herstellung von Na-Beta-Aluminat-Keramiken über die Festkörperreaktion geeigneter Präkursoren wurde systematisch untersucht. Dabei wurde ausgehend von verschiedenen Rohstoffen, die Prozesskette von der Pulveraufbereitung bis zur Sinterung analysiert. Es wird gezeigt welchen Einfluss die verschiedenen Parameter auf die Ausbildung des Phasenbestands haben und letztendlich auf die elektrochemische Performance der Batterie ausüben können.

1 EINLEITUNG

Der Ausbau regenerativer [1] und der Rückbau fossiler sowie nuklearer Energieträger generieren völlig neue Anforderungen an die vorhandene Netz-Infrastruktur [2; 3]. Der „mismatch“ zwischen saisonaler und regionaler Energieerzeugung und dem Energieverbrauch erfordert „neue“ Netzarchitekturen. Ein wesentlicher Bestandteil dieser „neuen“ Netze sind Energiespeicher zur Netzstabilisierung [4; 5].

Aufgrund ihrer hohen Energiedichte, der guten Zyklenstabilität, der guten Verfügbarkeit der erforderlichen Rohstoffe und ihrer geringen ökologischen und ökonomischen Belastung sind Na-basierte Hochtemperatur-Batterien prädestiniert für die großformatige stationäre Energiespeicherung [6; 7]. Die energiepolitische Entwicklung und die guten Eigenschaften der Hochtemperaturbatterien führten in jüngster Vergangenheit zu einer starken Zunahme der Entwicklung auf dem Gebiet der Na-Beta-Aluminat-Keramiken [8].

Neben der Temperatur wird die Leistungsfähigkeit der Batterien in hohem Maße durch die Eigenschaften der Na-Beta-Aluminat-Keramik bestimmt. Dabei nimmt deren Herstellung einen wichtigen Stellenwert ein [9]. So werden in der Literatur diverse Syntheserouten beschrieben [10–12], deren Ziel i. d. R. die Erhöhung der Na-Ionen-Leitfähigkeit oder der Festigkeit ist. Dabei variieren die verwendeten Rohstoffe, die chemische Zusammensetzung und die Prozessparameter. Die Mikrostruktur [13], der Phasenbestand und damit wesentliche elektrochemische Eigenschaften der Keramik werden so gezielt optimiert.

Die allgemeine stöchiometrische Zusammensetzung des Natrium-Beta-Aluminats kann mit $Na_2O \cdot x\text{-}Al_2O_3$ beschrieben werden. Abhängig von der eingestellten Zusammensetzung nach dem Sintern (x = 5 - 11) ist es möglich, natriumreiche bzw. natriumarme Phasen im Gefüge zu finden. Hierbei wird im Wesentlichen zwischen der ß und ß“ Phase unterschieden. Ziel des Synthesevorganges ist es jedoch, die ß-Phase (welche sich anfänglich bildet) vollständig in die ß“-Phase umzuwandeln, da diese eine wesentlich höhere Leitfähigkeit für Natriumionen aufweist. Werden jedoch im Sinterregime Temperaturen von 1500 °C überschritten [14], wird diese Phase instabil und zersetzt. Um diesem Phänomen entgegen zu wirken, ist es üblich sogenannte Stabilisatoren in die Verbindung mit einzubringen. Hierbei wird beispielweise Lithium- bzw. Magnesiumkarbonat oder gar eine Mischung aus beiden zugegeben [15].

2 EXPERIMENTELLES VORGEHEN

Die Synthese der Na-Beta-Aluminat-Keramiken erfolgte durch die „klassische“ Festkörperreaktion. Die chemische Zusammensetzung des Na-Beta-Aluminats wurde wie folgt gewählt.

$$(Al_{11-y}M_yO_{16})(Na_{1+2y}O) \text{ mit } y = 0{,}3 \text{ und } M = Li \text{ bzw. } Mg$$

Bei der Synthese wurden zwei verschiedene Ansätze hinsichtlich der strukturstabilisierenden Bestandteile verfolgt. Der Einfluss aus der Li oder Mg-Stabilisierung auf die Phasenbildung wurde so erfasst. Die verwendeten Ausgangsmaterialien waren Boehmit (AlO(OH)), Na_2CO_3 als Natriumquelle sowie Li_2CO_3 bzw. $4MgCO_3 \cdot Mg(OH)_2 \cdot H_2O$ als stabilisierende Bestandteile.

Die der Stöchiometrie entsprechenden Mengen der Ausgangsmaterialien wurden in einer Planetenmühle unter Zugabe von wasserfreien Ethanol für 1 h gemeinsam gemahlen und homogenisiert. Nach dem Trocknen wurden Pulverproben bei Temperaturen von 1100, 1200 und 1300 °C an Luft für jeweils 2 h in ZrO_2-Tiegeln getempert. Anschließend wurden die getemperten Pulver hinsichtlich des Phasenbestands durch Röntgenbeugung, der Kornform (REM) und Korngrößenverteilung (Laserbeugung) charakterisiert.

Nach dem Tempern der Pulver lagen sehr feine Pulver mit einem mittleren Korndurchmesser von 1,6 µm vor. Aufgrund ihrer Plättchen-förmigen Kornform neigen die Pulver strak zur Bildung von Agglomeraten.

Thermische Effekte, die während des Kalzinier- und Sinterprozesses der verschiedenen Ausgangspulver (Präkursoren) auftreten können, wurden mittels Differenzthermogravimetrie (DTG) und Thermomechanischer Analyse (TMA) am SETARAM 92-16 untersucht. Zur DTG-Messung wurden Platintiegel mit etwa 45 g der Pulver gefüllt, für die TMA-Messung wurden zylindrische Proben (Ø = 5 mm und L = 25 mm) der jeweiligen Pulver mittels uniaxialen Pressverfahren mit 4 bar hergestellt (ohne

Presshilfsmittel). Beide Messungen wurden anschließend jeweils unter Luftatmosphäre durchgeführt, wobei die Proben mit 2 K/min auf 1500 °C geheizt wurden.

3 Ergebnisse und Diskussion

3.1 Thermische Analysen zum Kalzinier- und Sinterverhalten

In Bild 1 und Bild 2 sind die Ergebnisse aus DTG und TMA-Messungen zusammenfassend dargestellt. Durch die geringe Heizrate von 2 K/min konnten bei der DTG und TMA die Präkursoren (Li- wie auch Mg-stabilisierte Proben) so temperiert werden, dass sich einzelne Effekte, die dem Kalzinieren und dem Sintern zugeordnet werden können, detailliert darstellen ließen. Generell zeigten sich ähnliche Verläufe bei den DTG- und TMA-Messungen der Li- und Mg-stabilisierten Proben (siehe Bild 1 und Bild 2). Es konnten nahezu identische Peaklagen bei Dehydration und der Zersetzung bestimmter Probenbestandteile zugeordnet werden. Untersuchungen von van Zyl et al. [16] zeigen vergleichbare Ergebnisse.

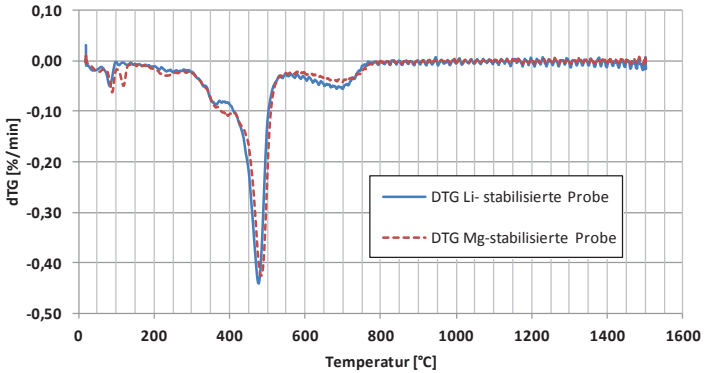

Bild 1: Massenänderung der Mg- und Li-stabilisierten Proben (DTG)

Anfänglich kommt es zu einer Wasserabspaltung aus dem Festkörper und Oberfläche der Probe (bei etwa 90 °C). Im Gegensatz zur Li-stabilisierten Probe vollzieht sich die Abgabe des Wassers bei der Mg-stabilisierten Probe in zwei Schritten, bei etwa 90 und 110 °C. Die ist auf die Abgabe des Kristallwassers aus dem $4MgCO_3 \cdot Mg(OH)_2 \cdot 5H_2O$ zurückzuführen. Die weitere Zersetzung von Li_2CO_3, Na_2CO_3 und auch $4MgCO_3 \cdot Mg(OH)_2$ findet im Temperaturbereich zwischen 300 und 400°C statt. Im weiteren Verlauf vollzieht sich der Phasenübergang von Böhmit zu γ-Al_2O_3 (400 - 550 °C). γ-Al_2O_3 ist eine Zwischenphase im System Böhmit-Li_2CO_3-Na_2CO_3 [16], aus der anschließend ß-Al_2O_3 gebildet wird. Eine starke Volumenausdehnung, wie sie bei anderen Zwischenphasen durch rekonstruktive Pha-

senumwandlungen auftritt (z. B. bei α-Al_2O_3 in der ß“-Bildung) kann hierbei nachweislich vermieden werden und wird als wesentlicher Vorteil in diesen Prozess gesehen.

Die eigentliche Phasenumwandlung zum ß“-Al_2O_3 während des Bildungsprozesses hängt vorrangig vom Temperaturprogramm, wie auch von den Stabilisierungselementen (Mg und/oder Li) ab. Der hier zu verzeichnende Unterschied zwischen den beiden Stabilisierungssystemen liegt in der temperaturabhängigen ß“-Bildung. In den vorliegenden Fall ist davon auszugehen, dass im Mg-stabilisierten System (Bild 2) der Hauptanteil von ß“-Al_2O_3 bereits bis 1200 °C gebildet wird. Hingegen vollzieht sich die ß“-Al_2O_3-Bildung im Li-System über zwei Schritte, bei dem ein erster Teil bis 1200 °C gebildet wird und der Hauptteil erst im Temperaturbereich 1500 - 1600 °C entsteht [15]. Neben der überlagerten Sinterung beider Proben wird dies speziell im Ausdehnungsverhalten der Li-stabilisierten Probe zwischen 1200 und 1500 °C deutlich (Bild 2).

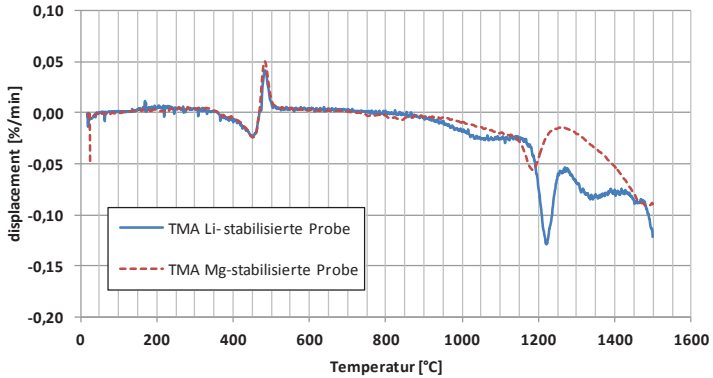

Bild 2: Thermische Dehnung der Mg- und Li-stabilisierten Proben (TMA)

3.2 Röntgenographische Phasenanalyse

In Bild 3 und Bild 4 sind die Röntgen-Diffraktogramme der Pulver, welche bei 1100 °C bis 1300 °C getempert wurden, vergleichend dargestellt. Bei 1100 °C ist unabhängig von der Dotierung eine beginnende Phasenbildung von Na-β“-Al_2O_3 zu erkennen. Für die Mg-stabilisierten Pulver ist die Phasenbildung bei 1300 °C abgeschlossen, was durch die DTA-Analysen bestätigt wird. Es liegt ein quasi einphasiges Na-β“-Al_2O_3 vor. Die Li-stabilisierten Pulver zeigen ein ähnliches Verhalten bezüglich der Phasenbildung. Bis zur maximalen Kalziniertemperatur von 1300 °C ist allerdings deutlich eine Nebenphase detektierbar. Ausgehend von den Ergebnissen der TMA-Analyse ist durch das Kalzinieren der Probe bei erhöhten Temperaturen ist eine Umwandlung der Nebenphase in Na-β“-Al_2O_3 zu erwarten.

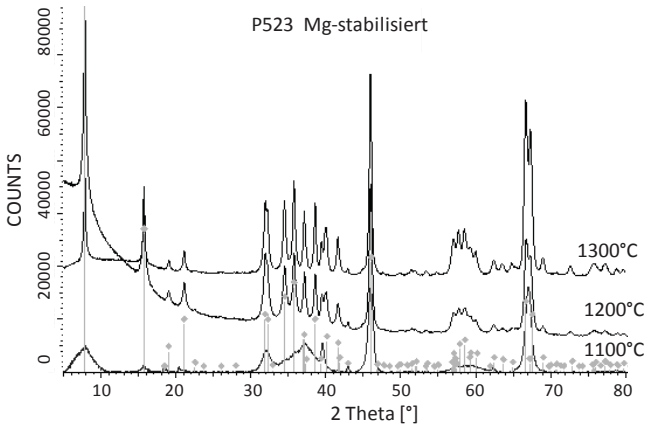

Bild 3: Röntgen-Diffraktogramme Mg-stabilisierter Na-Beta-Aluminat-Pulver getemperte bei verschiedenen Temperaturen.

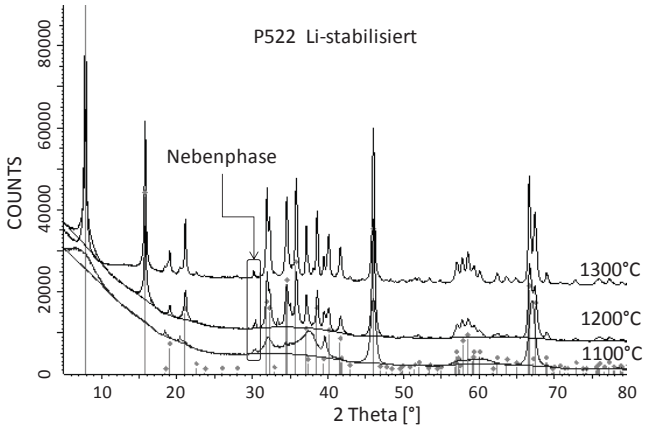

Bild 4: Röntgen-Diffraktogramme Li-stabilisierter Na-Beta-Aluminat-Pulver getemperte bei verschiedenen Temperaturen.

4 ZUSAMMENFASSUNG

Durch „klassische“ Festkörperreaktion wurden ausgehend von Boehmit und Na_2CO_3 Na-Beta-Aluminatkeramiken synthetisiert. Als stabilisierende Komponenten wurden

dabei Li_2CO_3 und $4MgCO_3 \cdot Mg(OH)_2 \cdot 5H_2O$ verwendet. Durch Untersuchungen mittels DTG, TMA und Röntgendiffraktometrie wurde die Phasenbildung in Abhängigkeit von der Kalzinierungstemperatur und der stabilisierenden Komponente untersucht. Es zeigte sich, dass die Mg-Stabilisierung bereits bei 1200 °C zu einem quasi einphasigen Na-ß“-Aluminat führt. Die Li-Stabilisierung weist bis 1300 °C noch Fremdphasen auf. Durch TMA-Messungen bis 1500 °C konnte die weitere Umwandlung in Na-ß“-Aluminat nachgewiesen werden. Grundsätzlich kann bei der Synthese des ß-Aluminats zwischen der Kalzinierung und einer anschließenden Sinterung unterschieden werden. Durch die vorgeschaltete Kalzinierung sollte die Bildung des Na-β“-Aluminats weitgehend abgeschlossen sein. Somit ist eine weitere Bearbeitung der Pulver (Granulierung, Mahlung) und damit ein besseres Sinterverhalten und optimierte Gefüge für leistungsfähigere Elektrolyten zu erwarten.

Danksagung

Wir danken der Thüringer Aufbaubank für die Förderung im Rahmen einer Thüringer Forschergruppe (2011 FGR 0089).

References

[1] Büsgen, U.; Dürrschmidt, W. The expansion of electricity generation from renewable energies in Germany: A review based on the Renewable Energy Sources Act Progress Report 2007 and the new German feed-in legislation, Energy Policy, 7 (2009) 2536–2545
[2] Anderson, D.; Leach, M. Harvesting and redistributing renewable energy: on the role of gas and electricity grids to overcome intermittency through the generation and storage of hydrogen, Energy Policy, 14 (2004) 1603–1614
[3] Zhenguo, Y.; Jianlu, Z.; Kintner-Meyer, M. C. W.; Lu, X.; Daiwon, C.; John P., L. Electrochemical Energy Storage for Green Grid, Chem Rev., 111 (2011) 3577–3613
[4] Connolly, D.; Lund, H.; Mathiesen, B.; Pican, E.; Leahy, M. The technical and economic implications of integrating fluctuating renewable energy using energy storage, Renewable Energy, 0 (2012) 47–60
[5] Doughty, D. H.; Butler, P. C.; Akhil, A. A.; Clark, N. H.; Boyes, J. D. Batteries for Large-Scale Stationary Electrical Energy Storage, The Electrochemical Society Interface, (2010) 49–53
[6] Dustmann, C.-H. Advances in ZEBRA batteries, Journal of Power Sources, 1–2 (2004) 85–92
[7] Sudworth, J. The sodium/nickel chloride (ZEBRA) battery, Journal of Power Sources, 1–2 (2001) 149–163
[8] Liu, J.; Zang, J.; Yang, Z.; Lemmon, J.; Imhoff, C.; Graff, G.; Li, L.; Hu, J.; Wang, C.; XIAO, J.; Xia, G.; Viswanathan, V.; Baskaran, S.; Sprenkle, V.; Li, X.; Shao, X.; Schwenzer, B. Materials science and materials chemistry for large scale electrochemical energy storage: from transportation to electrical grid, Adv. Func. Mater, (2012) 1–18
[9] Lu, X.; Xia, G.; Lemmon, J.; Yang, Z. Advanced materials for sodium-beta alumina batteries: Status, challenges and perspectives, Journal of Power Sources, 9 (2010) 2431–2442
[10] Sartori, S.; Martucci, A.; Muffato, A.; Guglielmi, M. Sol-gel synthesis of Na- beta-Al_2O_3 powders, Journal of the European Ceramic Society, 6 (2004) 911–914
[11] Park, H.; Lee, Y.; Lee, S.; Lee, C.; Kim, J.; Hong, S.; Park, S. Synthesis of beta-alumina powders by microwave heating from solution-derived precipitates, Ceramics International, 2 (2005) 293–296
[12] Jayaraman, V.; Periaswami, G.; Kutty, T. Gel- to -crystallite conversion technique for the syntheses of M-β/β″-alumina (M = Li, Na, K, Rb, Ca or Eu), Materials Research Bulletin, 10 (2008) 2527–2537

[13] Sakka, Y.; Honda, A.; Suzuki, T.; Moriyoshi, Y. Fabrication of oriented β-alumina from porous bodies by slip casting in a high magnetic field, Solid State Ionics, 1–4 (2004) 341–347
[14] Kasli, H.; Tandon, R.; Balbir, S.; Goel, R.; Das, B. Preperation and characterisation of ß“-Al2O3, Bull. Mater. Sci., 6 (1984) 979–989
[15] Park, J.; Kim, K. Influence of stabilizers on Na-ß“-Al_2O_3 phase formation in Li_2O(MgO)-Na_2O-Al_2O_3 ternary systems, Journal of Materials Science, 33 (1998) 5671–5675
[16] Zyl, A.; Thackeray, M.; Duncan, G.; Kingon, A. The synthesis of beta alumina from hydroxide and oxyhydroxide precursors, Mat. Res. Bull., 28 (1998) 145–157

Electrochemical behavior of Si nanostructures in ionic liquids

C. Vlaic[1], C. Hühn[2], L. Grohmann[2], L. Schulze[2], S. Ivanov[1]*,
D. Wang[2], P. Schaaf[2], A. Bund[1]

[1] Ilmenau University of Technology, Institute of Materials Engineering, Chair Electrochemistry and Electroplating, Gustav-Kirchhoff-Straße 6, D-98693 Ilmenau (Germany)
[2] Ilmenau University of Technology, Institute of Materials Engineering, Chair Materials for Electronics, Gustav-Kirchhoff-Straße 5, D-98693 Ilmenau (Germany)

* corresponding author: Svetlozar-Dimitrov.Ivanov@tu-ilmenau.de

Abstract

In the present work silicon nanostructures with a grass–like morphology were investigated using cyclic voltammetry and galvanostatic measurements in 1 M Li^+TFSI^- lithium bis(trifluoromethanesulfonyl)imide in N-butyl-N-methyl-pyrrolidinium bis(trifluoromethane-sulfonyl)imide ([BMP][TFSI]). The samples were p-type and n-type Si with different doping levels and different crystallographic orientations. Nanostructuring of the silicon resulted in an enhanced electrochemical Li-ion exchange for all the samples. The best cycling performance was obtained for the sample with the highest conductivity, while the crystallographic orientation had a less important contribution. SEM investigations of electrode surfaces showed significant morphological changes after extended potential cycling.

1 INTRODUCTION

Lithium-ion batteries are the power sources of choice for the portable electronic market [1] and nowadays there is a huge interest for lithium-ion batteries with higher specific capacity and power density, e.g. for implementation in electric vehicles. Silicon is considered to be one of the next generation anode materials, since it has a very high theoretical specific charge capacity (4200 mAh/g) [2]. However, it suffers large volume changes (>300%) during the alloying/dealloying processes resulting in pulverization of the electrode material and rapid fading of the cell capacity. One approach for solving this problem is to decrease the silicon dimensions to submicrometers or nanometers which allows for better accommodation of the mechanical stress in the structure. At the same time, ionic liquids (ILs) attract considerable interest due to their exceptional properties (wide electrochemical windows, low volatility and low flammability) which make them suitable electrolyte systems for high energy, rechargeable batteries [3]. Hence, the use of nanostructered silicon anodes in combination with IL based electrolytes may be highly advantageous for novel, high power and energy density Li batteries with excellent safety characteristics.

2 EXPERIMENTAL DETAILS

In the present work different silicon nanostructures were investigated in 1 M Li^+TFSI^-, [BMP] [TFSI]. The samples were p- and n-type Si with different doping levels and crystallographic orientations: (100) and (111) with a grass-like surface morphology. The nanostructured silicon samples tested during the cyclic voltammetry experiments were: Sample A: (100) p-type, 6-10 Ω·cm; sample B: (111) p-type, 0.001 Ω·cm; sam-

ple C: (111) n-type 0,017 Ω·cm. The nanograss structure of the Si interface was processed using the self-masked reactive ion etching (RIE) with a SF_6/O_2 plasma. During the etching process, the passivation material (SiO_xF_y) was deposited on the surface and acted as masking spots, leading to the nano-grass structure. The Si wafer is black due to the surface modification with very low reflectivity and correspondingly high absorption of visible light.

The samples were electrochemically characterized using a potentiostat/galvanostat (Biologic VMP3) in a three electrode configuration. They were voltammetrically cycled within a potential range 2.5 V – 0.02 V vs. Li/Li^+ with a scan rate of 0.5 $mV \cdot s^{-1}$. The galvanostatic measurements were carried out at different constant current values with cut-off voltage window between 1 and 0.1 V. A home-made PTFE electrochemical cell equipped with Li metal counter and reference electrodes was used for electrochemical tests. The cell assembly and electrochemical measurements were performed in a glove-box (MBraun, Garching, Germany) maintaining H_2O and O_2 levels below 0.1 ppm. The samples were investigated using an ultrahigh resolution scanning electron microscope (FE-SEM, Hitachi S-4800).

3 RESULTS

3.1. Cyclic voltammetry experiments

Cyclic voltammetry of the Si samples and the corresponding flat reference electrodes was carried out (Fig. 1). The voltammetric behaviour of the three samples was compared between each other and with the reference Si material. From the currents registered during the CV measurements it can be observed that generally, “black Si” displays higher voltammetric currents compared to the reference samples. From the three sample investigated, B shows the the highest charge capacity, almost twice that of sample A and sample C (Fig. 1).

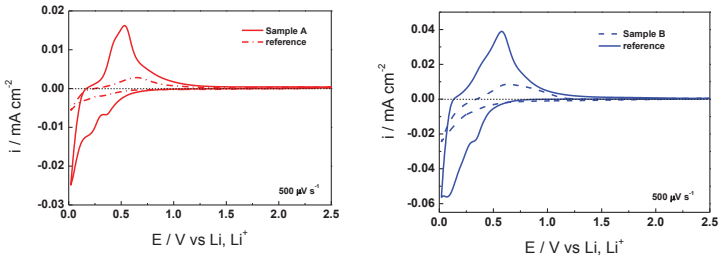

Fig 1. Cyclic voltammetry for samples A and B and the corresponding reference samples in 1M Li BMP TFSI between 0.02 V and 2.5 V, scan rate 0.5 mV/s

Based on this result, sample B was further investigated in a long time test during 110 consecutive cycles (Fig. 2). A maximum discharge capacity was reached at the 40th cycle after which a decrease in the values was registered. The capacities calculated on the basis of the cyclic voltammetry experiments for the reference sample and for sample B during 40 cycles and also for the long time experiment are presented in Fig. 2.

The sharp increase of the capacity around the 10th cycle in the long time test can be attributed to possible cracks that occurred in the electrode material.

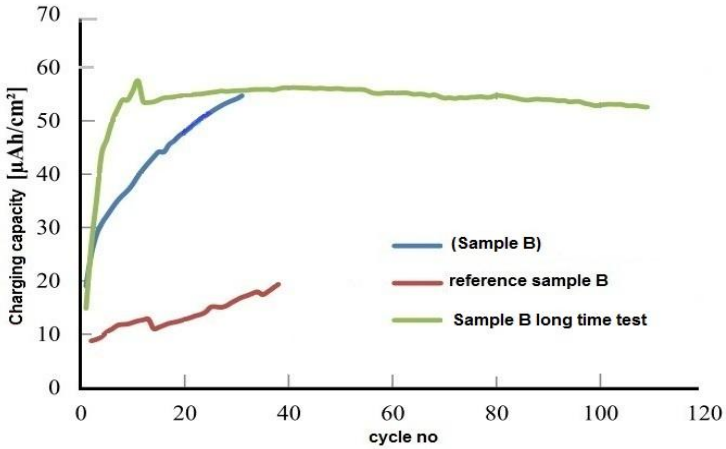

Fig 2. Charging capacity for the reference sample (40 cycles) and sample B (40 and 110 cycles)

3.2. Galvanostatic measurements

As discussed already sample B displayed superior performance and therefore was selected for galvanostatic tests. A constant decrease for the discharge capacity of the nanograss was registered for current values between 40 μA and 5 μA. The decrease of the charge capacity can be explained by the fact that the electrode material is progressively cracked during consecutive charging and discharging cycles.

3.3. SEM imaging

Figure 3 presents SEM images for sample B before and after 110 voltammetric cycles. Initially all the three samples had a grass-like surface morphology. After the CV measurements the surface morphology of the silicon showed significant degradation and the initial nanostructures were no more discernible. The high number of cracks indicate that the investigated nanostructured silicon electrode does not accommodate

adequately the mechanical stress during long time charging and discharging processes. These cracks disintegrate the sample, but at the same time, they expose new active material with which Li ions can further react. The SEM images of samples A and C (images not shown) revealed that the nanostructures of the surface were also not visible after the cyclic voltammetry measurements. This could be due to the formation of a solid electrolyte interphase (SEI) on the electrode surface. Attempts to wash away the residues with ethanol and acetone were not successful.

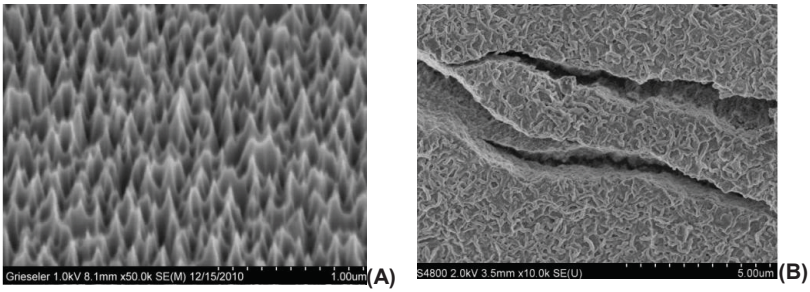

Fig 3. SEM images for sample B before (A) and after the long time test (B) by cyclic voltammetry in 1 M $Li^{+}TFSI^{-}$ [BMP][TFSI]

The depth of Li penetration in the active material was estimated from cross-section SEM images. The values obtained from these approximations were used to calculate the specific charge capacity for sample B which is about 16 $mAh \cdot cm^{-2}$. This value is relatively small compared to similar results in the literature [4].

4 DISCUSSION

The results obtained in the present work allow us to conclude that the nanostructuring of silicon in the form of nanograss enhances the charging capacity of this anode material for the lithium-ion batteries.

During the CV measurements it was observed that at the first silicon alloying/dealloying cycle, the electrolyte interacted with Li ions and the reaction products began to accumulate at the electrode interface and to build a SEI layer. This process was described also by Baranchugov et al. [3] who consider that at low potential values the TFSI anions undergo a reduction process that results in the deposition of an insoluble layer on the electrode surface. A second process that took place during the first voltammetric cycle was the transformation of crystalline into an amorphous state silicon material.

Besides the nanostructuring, the larger charge capacity obtained for sample B can be attributed as well to the enhanced conductivity of this sample. We also found that the crystal orientation of the silicon used for preparing the nanograss does not have a

strong influence on the electrochemical behaviour. This could be related to the fact that for all samples after the first CV cycles the crystalline silicon becomes amorphous and the contribution of the initial crystallographic orientation is less significant afterwards.

5 CONCLUSIONS

Silicon was nanostructured in the form of a grass-like morphology. Three samples of p-type and n-type Si with different doping levels and different crystallographic orientations: (100) and (111) were investigated by cyclic voltammetry and galvanostatic measurements in 1M Li^+TFSI^-, [BMP],[TFSI].

The sample obtained from 0.001 Ω·cm (111) p-type Si showed the highest capacity enhancement (relative to a flat Si substrate) due to its high conductivity. The effect of the crystallographic orientation seems to be minor since Si became amorphous during the first Li charging/discharging process. Unfortunately, the nanograss-like morphology of silicon does not accommodate adequately the mechanical stress during long time charging and discharging of Li ions.

Considering the first promising results obtained with silicon nanostructures, further studies will be carried out for investigating other nanosized morphologies such as nanoporous silicon or nanoporous nanopillar Si. These nanostructures are expected to better accommodate the volume changes during Li charging/discharging processes along with the enhanced charging capacity.

Acknowledgements

This work was supported by a grant (NanoBatt TNA VII-1/2012) from the state of Thuringia (TMWAT by LEG Thüringen) and co-financed by the European Union within the frame of the European Funds for Regional Development (EFRD).

References

[1] B. Scrosati, J. Hassoun, Y.-K. Sun: Lithium-ion batteries. A look into the future, Energy Environ. Sci., **4**, (2011), 3287.

[2] M. Ge, J. Rong, X. Fang, C. Zhou: Porous Doped Silicon Nanowires for Lithium Ion Battery Anode with Long Cycle Life, Nano Lett., **12**, (2012), 2318.

[3] V. Baranchugov, E. Markevich, E. Pollak, G. Salitra, D. Aurbach: Amorphous silicon thin films as a high capacity anodes for Li-ion batteries in ionic liquid electrolytes, Electrochem. Commun., **9** (2007) 796.

[4] M. Green, E. Fielder, B. Scrosati, M. Wachtler, J. S. Moreno: Structured Silicon Anodes for Lithium Battery Applications, Electrochem and Solid State Lett., **6**, (2003), A75.

INVESTIGATION OF PHOTONIC CRYSTAL LED COUPLING PROPERTIES USING SPECTROSCOPIC ELLIPSOMETRY

P. Hronec[1], J. Kováč[1], J. Škriniarová[1], S. Shokhovets[2], P. Schaaf[3]

[1] *Institute of Electronics and Photonics, Faculty of Electrical Engineering and Information Technology, Slovak University of Technology, Ilkovičova 3, 81219 Bratislava, Slovak Republic. (e-mail: pavol.hronec@stuba.sk)*

[2] *Institute of Physics, Faculty of Mathematics and Natural Sciences, Ilmenau University of Technology, Weimarer Str. 32, 98693 Ilmenau, Germany*

[3] *Institute of Materials Engineering, Department of Electrical Engineering and Information Technology, Ilmenau University of Technology, Gustav-Kirchhoff-Strasse 5, 98693 Ilmenau, Germany*

Abstract: The paper deals with a theoretical description of the $Al_{0.295}Ga_{0.705}As$/GaAs multi-quantum well light emitting diode structure as a planar waveguide and photonic crystal acting as coupling grating. For characterisation of the waveguide optical properties, spectral ellipsometric measurements were performed. The measurements show that photonic crystal patterned to the surface of the $Al_{0.295}Ga_{0.705}As$/GaAs multi-quantum well LED strongly affects its optical properties.

Keywords: Photonic crystal, Light-emitting diode, waveguide, MQW

1 INTRODUCTION

Light extraction efficiency (LEE) is the limiting factor in achieving high optical power output from light emitting diodes (LED) because a high fraction of the generated light is back reflected by total internal reflection at the GaAs - air interface. Therefore, plenty of efforts try to improve LEE which has also a positive environmental impact because of saving electrical energy. In the last years, the LEE improvement is employing an approach based on periodic structures, called photonic crystals (PhC), or photonic bandgap (PBG) crystals [1] patterned in the surface of the structure [2-3]. The PhC patterning in the LED surface is a very promising method for improving LEE and other properties. This study is focused on theoretical description of $Al_{0.295}Ga_{0.705}As$/GaAs light emitting diode (LED) as a planar waveguide completed by variable angle spectroscopic ellipsometry measurements of this structure with two dimensional photonic crystal structures patterned into the surface.

2 PHOTONIC CRYSTALS LED PROBLEM FORMULATION

Considered LED structure is $Al_{0.295}Ga_{0.705}As$/GaAs based structure with $Al_{0.295}Ga_{0.705}As$ active region consisting of three GaAs quantum wells. Structure arrangement with the thicknesses of layers is shown in Fig. 1. Central wavelength of the realized LED is measured near 845 nm. Active layer region acts like a core of the planar waveguide with $Al_{0.295}Ga_{0.705}As$ layers as a cladding. Emitted light from the active region is assumed to be a plane wave propagating in the planar waveguide.

Refractive index of the core consisting of the five layers of the two different materials can be approximated according to [4] using harmonic average of the n_i^2 for the TE mode and $1/n_i^2$ for TM mode, where i is the number of the layer with corresponding thickness l_i.

$$n_{feff,TE}^2 = \frac{\sum_i n_i^2 l_i}{\sum_i l_i} \qquad (1) \qquad\qquad \frac{1}{n_{feff,TM}^2} = \frac{\sum_i \frac{1}{n_i^2} l_i}{\sum_i l_i} \qquad (2)$$

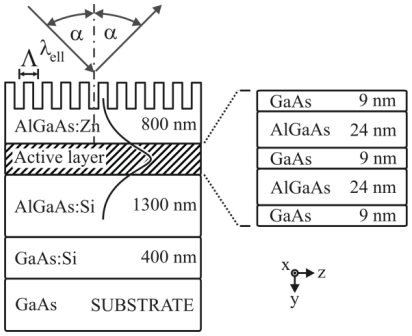

Fig. 1 Considered $Al_{0.295}Ga_{0.705}As$/GaAs LED structure with MQW waveguide active layer.

2.1 Planar waveguide

As is mentioned above this structure acts like a symmetrical planar waveguide because approximated refractive index of the active region is larger than refractive indices of identical surrounding $Al_{0.295}Ga_{0.705}As$ layers. Characteristic equations for planar waveguide according to [5] are

$$u_{TE}\, tg(u_{TE}) = q_{TE}, \qquad (3) \qquad\qquad -u_{TE} \cot g(u_{TE}) = q_{TE}, \qquad (4)$$

for TE modes and

$$u_{TM}\, tg(u_{TM}) = \frac{n_{feff,TM}}{n_{AlGaAs}} q_{TM}, \qquad (5) \qquad -u_{TM} \cot g(u_{TM}) = \frac{n_{feff,TM}}{n_{AlGaAs}} q_{TM}, \qquad (6)$$

for TM modes where normalized transverse wave numbers u and q are defined by means of half a height of guiding layer and wave vectors in y direction in guiding layer ($k_{y,f}$) and cladding layers ($k_{y,AlGaAs}$) as

$$u_j = a\, k_{y,f,j}, \qquad (7) \qquad\qquad q_j = a\, k_{y,AlGaAs,j}, \qquad (8)$$

where $j = TE,TM$. These normalized wave numbers are not independent but they are related by equation

$$u_j^2 + q_j^2 = k^2 a^2 (n_{feff,j}^2 - n_{AlGaAs,j}^2) = v_j^2. \qquad (9)$$

Then

$$v_j = \frac{\pi}{\lambda_0} h \sqrt{n_{feff,j}^2 - n_{AlGaAs,j}^2} \qquad (10)$$

and solutions of equations are normalized transverse wave numbers of the modes which can be guided in the waveguide.

$$u_j \, tg(u_j) = \sqrt{v_j^2 - u_j^2}\,, \qquad (11) \qquad -u_j \cot g(u_j) = \sqrt{v_j^2 - u_j^2} \quad (12)$$

Then propagation angle can be expressed as

$$\theta_j = arctg \frac{\sqrt{k_0^2 n_{feff,j}^2 - \left(\frac{u_j}{a}\right)^2}}{\left(\frac{u_j}{a}\right)}, \qquad (13)$$

where k_0 is wave vector in the vacuum

2.2 Coupling from corrugated waveguide using 1D PhC

For coupling the guided modes to the air the one dimensional (1D) periodic structure is typically used (Fig. 2). It is patterned in the cladding layer of the waveguide and diffracted guided modes according to general phase-matching condition

$$\frac{2\pi}{\Lambda} m = \beta_1 - \beta_2 \qquad (14)$$

where m is diffraction order, Λ is grating period, β_1 is incident light wave vector and β_2 is diffracted light wave vector. To achieve diffraction direction perpendicular to incident light direction the first order diffraction has to be obtained. [5] Directions of these wave vectors are shown in Fig. 3. However this process is symmetrical, also for light coupling from air to the core of the waveguide, this phase matching condition must be satisfied.

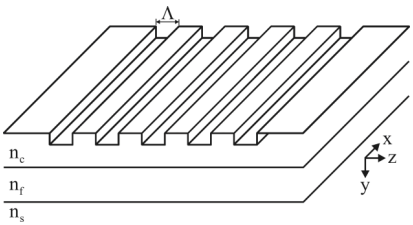

Fig. 2 Illustration of coupling 1D grating patterned in the cladding layer of the waveguide for characterization of mode extraction.

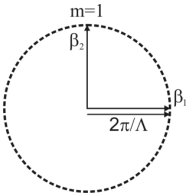

Fig. 3 Direction of incident and first-order diffracted wave vector in structure described above. (Okamoto, 2006) Light is diffracted perpendicular to incident light when z-direction wave vector of guided mode and wave vector of the coupling grating are equal.

2.3 2D photonic crystal

Coupling grating shown in Fig. 2 is simple 1D PhC which couples light from air to the waveguide. But measured LED structure has patterned 2D photonic crystal. It is the simplest 2D PhC which uses square symmetry with two characteristic directions denoted as ΓX or ΓM direction. The grating period Λ was approximately 500 nm and circular shaped air holes were prepared using interference lithography with etching depth approximately 200 nm. Each direction acts like a 1D grating and also ellipsometric measurements were made for both directions separately. Real and reciprocal lattice of this structure with Brillouin zone is shown in Fig. 4.

3 ELLIPSOMETRIC MEASUREMENTS

The spectroscopic ellipsometry parameters can be used to characterize PBG structures because of the relationship between different polarization states. Ellipsometers in general can measure *tan(Ψ)* and *cos(Δ)* or Ψ and Δ, respectively. These parameters are defined as [7]

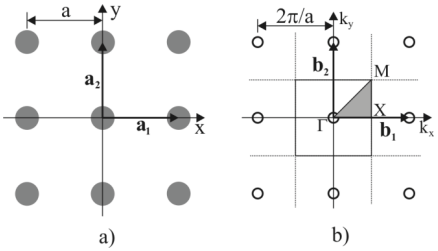

Fig. 4 Representation of the a) real and b) reciprocal lattice with Brillouin zone of 2D PhC with square symmetry. [6]

$$\tan(\psi)e^{j\delta} = \frac{E_{r,TM}/E_{i,TM}}{E_{r,TE}/E_{i,TE}} = \frac{\rho_{TM}}{\rho_{TE}} \qquad (15)$$

$$\tan(\psi) = \left|\frac{\rho_{TM}}{\rho_{TE}}\right| \qquad (16)$$

$$\cos(\delta) = real\left(\frac{\rho_{TM}/\rho_{TE}}{|\rho_{TM}/\rho_{TE}|}\right) \qquad (17)$$

Spectral dependence of ellipsometric parameters measured at three different angles of incidence α for the LED structure without PhC is shown in Fig. 5. There are peaks and dips in *tan(Ψ)* spectrum due to the interference between particular layers of the multilayered structure. Spectral dependence of the ellipsometry measurements of the PhC LED in ΓX and ΓM directions are shown in Fig. 6 and Fig. 7 respectively. From these two figures it can be clearly seen that peaks and dips invoked by interference still remain but there are additional peaks and dips (labelled with black ellipses) which originate from different reflection coefficients of TE and TM modes for investigated PhC. This means, that the high reflection coefficient of TM modes in comparison to the TE modes reflection coefficient is responsible for peaks and high reflection coefficient of TE modes in comparison to the TM modes reflection coefficient is responsible for dips. The difference in reflection originates from the bands in pho-

tonic band diagram of PhC for TE and TM modes according to Ref. [7]. Then, TE bandgaps would appear as a dip in the *tan(Ψ)* spectrum and TM bandgaps would lead to the peak value of *tan(Ψ)*. But there is also another phenomenon, which should be taken into account especially for structures like the investigated $Al_{0.295}Ga_{0.705}As/GaAs$ multi-quantum well LED whose approximated refractive index [4][8][9] of active layer is higher than the refractive index of ambient layers. Such an active layer acts like a core of the planar waveguide with $Al_{0.295}Ga_{0.705}As$ layers as a cladding [9][10]. Thus PhC patterned in the LED surface acts like a coupling grating [5][11], which can couple incident light from ellipsometer to the waveguide. So this means that peaks in the *tan(Ψ)* spectrum indicate coupling of the TE modes and dips indicate coupling of the TM modes into the waveguide. Process of the coupling must satisfy condition that tangential component of wave vector in the air, photonic crystal and coreof the waveguide is equal. This can be expressed by equation

$$k_{air}.sin(a) = k_{PhC} = k_{Core}.sin(\theta_j), \qquad (18)$$

where k_{air}, k_{PhC}, k_{Core} is wave vector in air, photonic crystal and core of the waveguide respectively, α is incident wave angle from ellipsometer and θ_j is propagation angle for appropriate guided mode (Eq. 13).

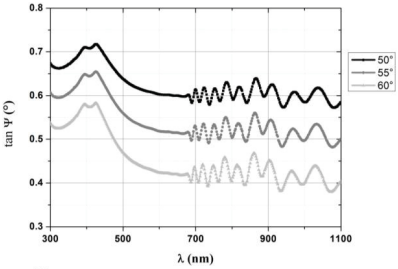

Fig 5 Spectral dependence of ellipsometric parameter *tan(Ψ)* for LED without PhC for different angles.

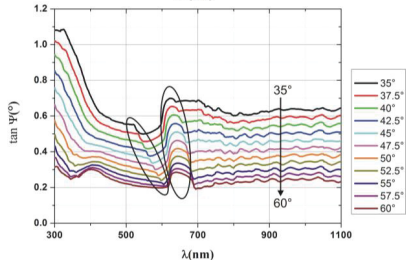

Fig 6 Spectral dependence of ellipsometric parameter *tan(Ψ)* for PhC LED in ΓX direction for different angles.

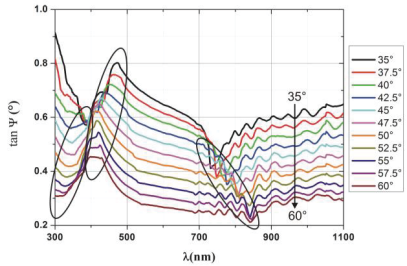

Fig. 7 Spectral dependence of ellipsometric parameter *tan(Ψ)* for PhC LED in ΓM direction for different angles.

4 CONCLUSIONS

Theoretical description of the 2D photonic crystals etched to the top of the $Al_{0.295}Ga_{0.705}As$/GaAs MQW LED and the measurements of their properties by spectroscopic ellipsometer are presented. For the presented structure the active region consisted of three quantum wells can be approximated by effective refractive index and thus the whole structure acts like a planar waveguide. Analysis of the *tan(Ψ)* spectrum showed that a PhC patterned surface strongly affects the polarization properties of the investigated sample. By comparison of the structures with and without the PhC there is possible to specify which peaks and dips in the spectra are invoked by PhC, which indicates TE or TM modes coupling. Based on these results, forthcoming studies should reveal the relation of photonic band gaps and ellipsometric spectra. It was also shown, that individual layers of the investigated structure create a waveguide with the active layer as a core and thus PhC can couple modes to this waveguide which has also effects on the polarization behaviour of the sample measured by ellipsometry and this effect should be taken into account in a next exact ellipsometric analysis.

ACKNOWLEDGMENT

This work was financially supported by VEGA project 1/0689/09 with bilateral cooperation with a DAAD project Ilmenau-Bratislava (DAAD PPP Schaaf NanoMat, 50755200).

REFERENCES

[1] E. Yablonovitch, Phys. Rev. Lett. 58 (1987) 2059–2062.
[2] Pudiš, D., Šušlik, Ľ., Kubicová, I., Škriniarová, J., Martinček, I. Advanced optical methods for patterning of photonic structures in photoresist, III-V semiconductors and PMMA. *Proc. of SPIE*, 7746, pp. 774616-1-6, 2010
[3] Kubicová, I., Pudiš, D., Šušlik, Ľ., Škriniarová, J., Slabeyciusová, S., Martinček, I. Structures patterning by non-contact NSOM lithography. *Proc. of SPIE*, 7746, pp. 774608-1-6, 2010
[4] Alman, G. M., L. A. Molter, H. Shen, M. Dutta: Refractive Index Approximations from Linear Perturbation Theory for Planar MQW Waveguides. *IEEE Journal of Quantum Electronics.* vol. 28, no. 3, pp. 650-657, 1992
[5] Okamoto, K., *Fundamentals of Optical Waveguides*, Chapter 2. Elsevier, USA, 2006
[6] Shen, Ch. *Wave Propagation through Photonic Crystal Slabs: Imaging and Localization*", Proefschrift, ISBN 90-367-2563-1, Groningen, Netherlands, 2006
[7] Hsieh, C. I., Chen, H. L., Chao, W. C., Ko, F. H.: Optical properties of two-dimensional photonic-bandgap crystals characterized by spectral ellipsometry. *Microelectronic Engineering*, vol. 73-74, pp. 920-926, 2004
[8] Saini, M., Sharma, E. K.: Equivalent Refractive Index of MQW Waveguides. *IEEE Journal of Quantum Electronics.* vol. 32, no. 8, pp. 1383-1390, 1996
[9] Sonek, G. J., Ballantyne, J. M., Chen, Y. J., Carter, G. M., Brown, S. W., Koteles E. S., Salerno, J. P.: Dielectric Properties of GaAs/AlGaAs Multiple Quantum Well Waveguides. *IEEE Journal of Quantum Electronics.* vol. QE-22, no. 7, pp. 1015-1018, 1986
[10] Hronec, P., Kováč, J.: Guided mode light extraction from LED structure using photonic crystals. *In Proc. of Elitech*, 2012, Bratislava, to be published
[11] Lifante, G.: *Integrated photonics: Fundamentals,* Wiley, ISBN 0-470-84868-5, England, 2003

A new method to characterize material properties of copper by microindentation

E. Aristizabal[1], F. Günter[1], P. Schaaf[2]

[1] Robert Bosch GmbH, Robert Bosch Str.2, 71701 Schwieberdingen, Germany
[2] Ilmenau University of Tecnology, Institute of Materials Engineering, Chair Materials for Electronics and Electrical Engineering, Gustav-Kirchhoff-Str.5, 98693 Ilmenau, Germany

Abstract

Cold-joined connectors are widely used, owing to the simplicity of the assembly process, the low initial investment, and the possibility to join several contacts in parallel. In addition, heat dissipation and contamination with flux does not occur in this joining process.

Due to the fast-growing number of high current applications in the automotive industry, increasing efforts are being made in order to make the advantages of the cold joining technology suitable for high currents. In parallel, new Finite Element Method models are still to be developed for the purpose of supporting the new design cycle.

Big cross sections needed for high current applications lead to high insertion forces, and thus, to a strong material damage in the contact zone. Thereof, new challenges arise both in terms of design and FEM simulation of the novel connectors.

FEM modeling of the insertion processes requires a good knowledge of the material properties in the contact area. The preferred technology to produce the assembly parts of cold joined connections is stamping. Stamping causes strong strain hardening in the contact zone and therefore alters the material properties significantly. Thus, material properties in the contact area differ significantly from the base material and have to be redefined.

This paper discusses new methods to characterize the elastic-plastic behavior of copper parts in the sphere of influence of the stamping process, by means of microindentation experiments.

1 INTRODUCTION

Most of the cold-joining technology since the 70s focused on the elastic deformation of one of the contact partners [1-3]. Nevertheless high current applications require large contact areas and thus massive contact partners have to be designed.

Cold joining connectors require very close tolerances for the assembly parts in order to get a stable joining process [2-3]. Stamping is the preferred manufacturing process to deliver the necessary reproducibility of the parts and to guarantee a robust assembly process. As shown in Fig. 1, the stamping process produces a high plastic strain in the material and therefore changes significantly the mechanical properties of the parts to be joined.

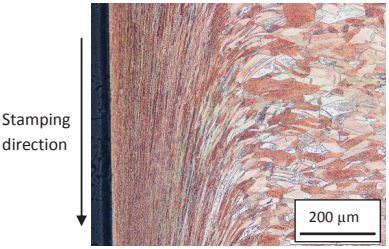

Fig. 1. Microstructure of CuSn015 affected by the stamping process

During the joining of massive high-current connectors, the insertion force is mainly absorbed by friction and plastic deformation of one or both contact partners in the contact zone. The contact zone of the parts has previously been altered by the stamping process. Knowing the mechanical properties of the joining parts close to the contact area is crucial for a correct understanding, design, and simulation of the joining process.

Microindentation is an accessible and suitable way of determining mechanical material properties in small material volumes. Therefore a new method is suggested to reevaluate the local material properties in strain-hardened zones as illustrated in Fig. 2.

The strength of the copper plates used to produce the cold joining connector is a design variable. As shown in Fig. 2, microindentation experiments have been used to find a correlation between hardness and mechanical properties using these commercial copper and bronze plates with different hardness. This correlation should deliver material properties that can be implemented on the existing FEM models.

On the other hand, the hardness in the area of influence of the stamping process has been screened. The above mentioned correlations will allow correlating the hardness screening with a distribution of different material properties that will be implemented in a FEM code.

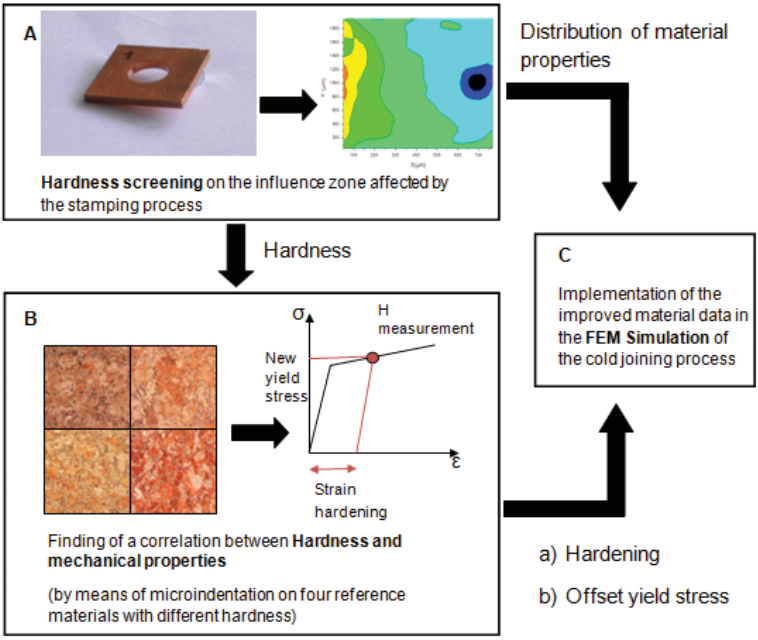

Fig. 2. Procedure to improve material data of the massive cold joining FEM Simulation

2 Experimental Details

Materials

The microstructures the four commercial samples are shown in Fig. 3. Three Cu-ETP rolled plates with different strengths (achieved by different heat treatments during/ after the rolling process) and a $CuSn_{015}$ alloy have also been used to find the correlation between the microindentation experiments and the elastic-plastic behavior of the materials.

Samples with identical chemical composition but different work-hardening levels will allow for a correlation between the hardness and the plastic behavior of the material. The $CuSn_{015}$ alloy will also be treated as a strain hardened pure copper.

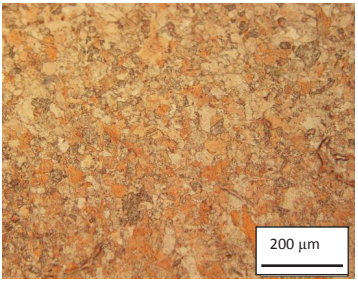

(a)

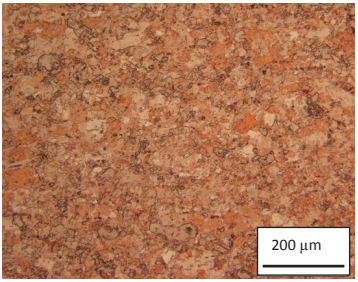

(b)

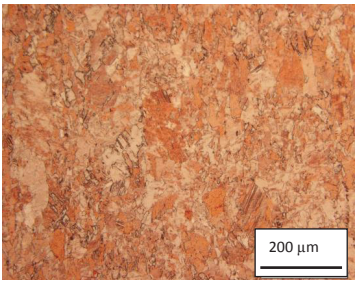

(c)

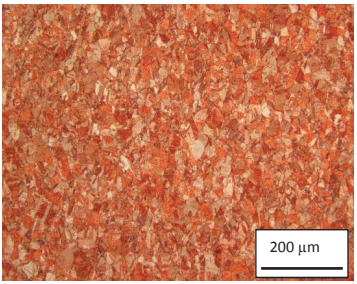

(d)

Fig. 3. Microstructure of the four studied materials. Micro-section: top view of the plate surface. Electrically etched with same parameters. (a) Cu-ETP R200, (b) Cu-ETP R250, (c) Cu-ETP R290, (d) $CuSn_{015}$ R290

Hardness measurements and tensile test in parallel and perpendicular to the rolling direction showed no clear anisotropic behavior of the specimens. Thus, a possible anisotropy due to the rolling direction of the plates has been neglected and different directions have been considered equal.

Tensile Tests

The true stress/ true strain constitutive behavior of the four materials has been determined using tensile tests.

The specimens for the tensile test have been produced according to DIN 5025:2009-07 and the plastic strain has been assessed with optic screening in order to obtain real strain data after the necking.

Three samples have been tested in the direction of rolling and three samples in the perpendicular direction for each material. The measurement uncertainty was for all materials under 1%.

Hardness Tests

Micro- and nanoindentation experiments have been widely used to characterize mechanical properties in work-hardened zones [4-7]. A correlation between the measured hardness and the effective strain allows characterizing the strength distribution along the not uniformly plastically deformed part. Several analytical approaches [7-23] and FEM Simulations [24-34] have been suggested to correlate effective strain with hardness.

Most procedures use continuous ball indentation to determine the stress/ strain behavior of the materials [7-16, 24-28], as it delivers information about the whole flow curve of the material in a single indentation.

On the contrary, the hardness, plastic strain and stress produced with a Vickers indenter is independent of the load, because of the self- similarity of the pyramid (disregarding the indentation size effect within the range of micro-hardness). Thus, only information of a single point in the flow curve can be obtained from a Vickers indentation.

The main source of measurement uncertainty is the sample preparation. Grinded and electropolished (unetched) surfaces deliver the best results.

A spherical Brinell indenter with D=0.4 mm was tested. Due to its geometry, the Brinell indenter produces superficial and big indentations. Thus, an indentation force of 1000 mN is necessary to get an indentation depth of about 2 μm and a measurement uncertainty below 5%. This procedure does not deliver the necessary resolution to get an exhaustive description of the hardness distribution in the small strain-hardened area.

Characterizing the hardness distribution in a small strain-hardened zone requires reliable measurements even for small loading forces, in order to get as many indentations as possible in the area to be studied.

Vickers indentation is replicable even with smaller loading forces and many indentations could be made in the strain-hardened area. That is why the Vickers indenter proved to be the most suitable alternative to characterize the influence area of the stamping process.

The loading force has been minimized in order to get as many indentations as possible. A loading for of 300 mN delivers a measurement uncertainty below 5% for the four materials. This force has been kept constant for all measurements.

The effect of the loading time was also studied, as show in Fig. 4. A shorter loading time induces a higher value of the hardness. This was to be expected due to the strain rate dependent behavior of copper. The strain rate dependency becomes critical for rates above 10^2 s^{-1}, but the effect is also noticeable for lower strain rates [45].

Nonetheless, the differences due to the strain rate are too small to be assessed with a measurement uncertainty that can reach 4%, as show in Fig. 5. Consequently, a loading time of 10 seconds has been kept constant for all measurements.

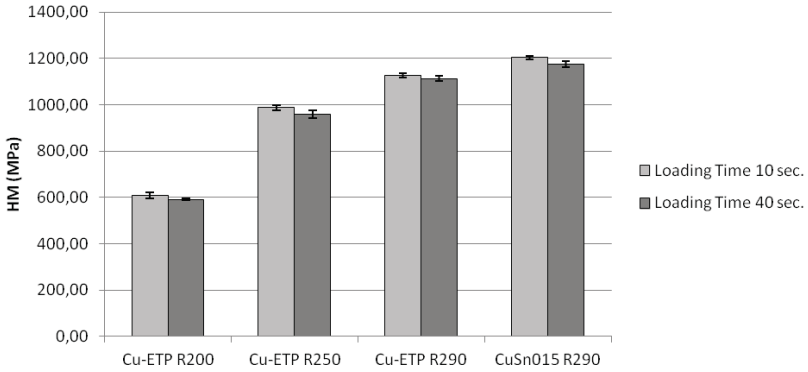

Fig. 4. Effect of the loading velocity on the Vickers Hardness (1000 mN)

The load-depth curves have been collected. Vickers hardness has been evaluated, as the goal is to correlate just the plastic component of the indentation with the flow curve.

3 RESULTS

Tensile tests

Tensile test provide the description of the true stress/ effective plastic strain relation of the four materials. The average of three measurements is show in Fig. 5a for each of the four specimens. The measurement uncertainty is in each case below 1%.

These results will set up the reference flow properties against which the results of the hardness measurements will be compared.

All materials show in the final stage of the flow curve the same constant hardening. The assumption of the specimens being the same material in different strain-hardened conditions is tested in Fig. 5b, assigning an initial plastic hardening to the flow curves. The strain-hardened curves have a higher yield stress than the one pre-

dicted with the assumption, due to the different thermal processes that they have been subjected to.

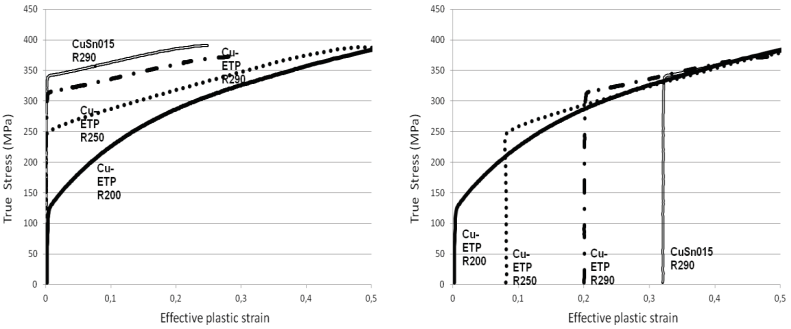

Fig. 5. (a)True strain/ true stress constitutive behavior of the studied materials. Results of the tensile tests. (b) Schematic representation of the flow curves of the different samples as strain-hardened specimens of the same material

Hardness screening on the strain-hardened area

Hardness screenings on the influence area of the stamping of real parts for cold joined connectors have been carried out, as represented in Fig. 6.

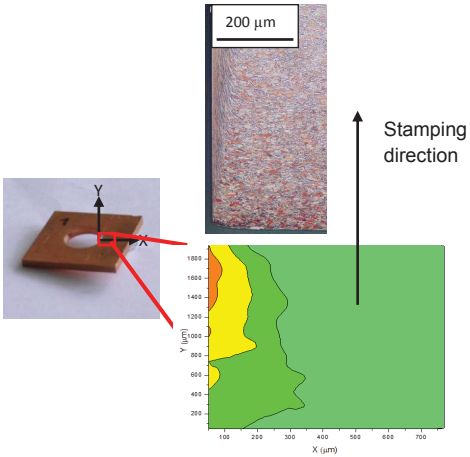

Fig. 6. Schematic representation of the hardness screening on stamped parts for cold joined connectors

The distance between indentations was kept according to ISO 6507-1. An indentation every 90 μm was made in Y direction and every 85 μm in X direction. The plots in Fig. 7 show the linearly interpolated results.

Plates made of each of the four reference materials have been tested.

The strain-hardened area by the stamping process and the hardness differences on the bulk material between the different specimens are visible in Fig. 7 (all plots have the same scale). The width of the strain hardened area decreases with the hardness of the balk material.

The hardness of the bulk material is in good agreement with the hardness specifications in the data sheet of the plates.

The stressed relieved sample, Cu-ETP R200 (Fig. 8 a), shows not only a clearly strain-hardened zone on the stamped edge, but also a rolling skin that has to be taken into account.

The second sample, Cu-ETP R250, has also a strain-hardened zone due to the stamping process. It is representative that the two softest materials show a higher hardness on the strain-hardened zone than the hardest reference material. This embodies once again the need of adequate description of material properties after the stamping process.

The hardness screen on the two hardest materials, Cu-ETP R290 and CuSn015 R290 shows a higher statistical spread (up to 10%) even in the zone X>400 μm, where the influence zone of the stamping has ended. More measurements have to be carried out in order to statistically assure a hardness distribution of both materials.

It is remarkable that the sample CU-ETP 290 shows a strain softening in the stamped edge. This could be a measurement artifact due to the sample preparation, as the electropolishing chamfers slightly the edges and may distort the measurements.

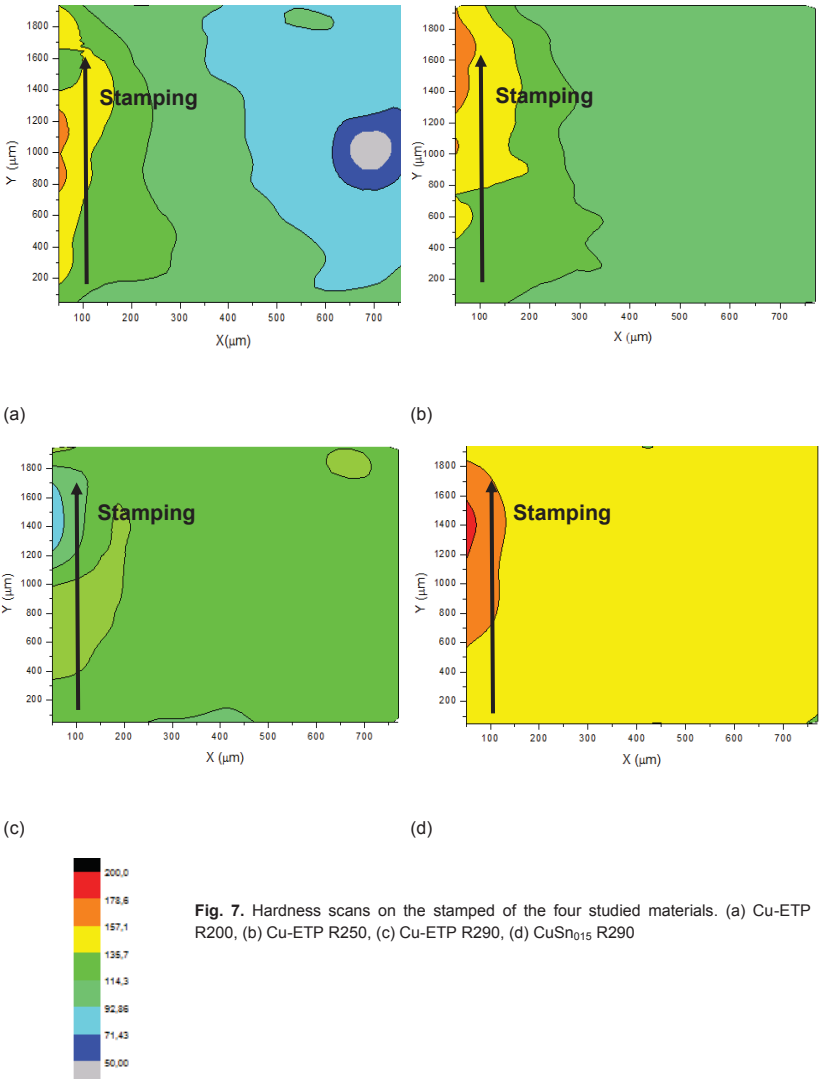

Fig. 7. Hardness scans on the stamped of the four studied materials. (a) Cu-ETP R200, (b) Cu-ETP R250, (c) Cu-ETP R290, (d) $CuSn_{015}$ R290

Hardness measurements on the reference materials

A representative load-depth indentation curve is represented in Fig. 8a as a mean curve of 15 measurements for the four different specimens. The corresponding HV values are indicated in Fig. 8b

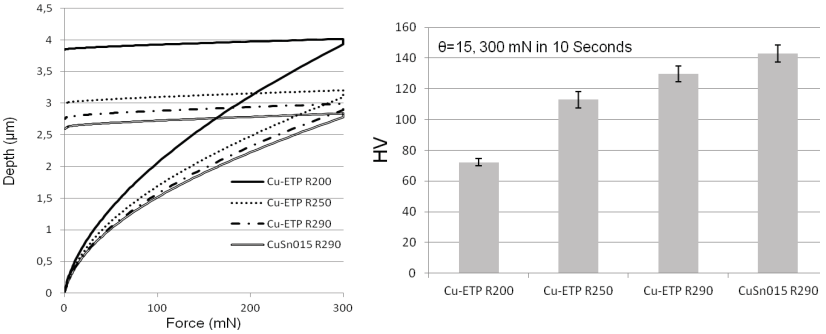

(a) (b)

Fig. 8. Hardness characterization of the four reference materials (a) Indentation load-depth curves, (b) Vickers Hardness

The hardness characterization of the materials was carried out in non-embedded specimens and the 2 mm copper plates were grinded and electropolished, so that the indentations do not take place on the rolling skin.

Nonetheless, the hardness screen (Fig. 7a) showed the presence of a distinctive rolling skin in the material Cu-ETP R200 (also represented in Fig. 9). This makes the hardness values measured as reference outside from the rolling skin not representative for a correlation with a tensile test since during a tensile test the whole cross section of the specimen is subjected to the same strain.

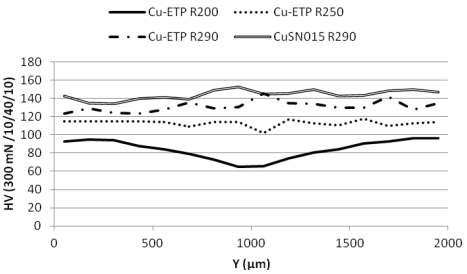

Fig. 9. Rolling skin. Material Cu-ETP R200

A representative hardness was calculated as shown in Eq. 1. The corrected hardness for Cu-ETP R200 is HV=739 MPa

$$H_{R200}=\frac{\int HdV}{V} \qquad \text{Eq. 1}$$

Although the sample Cu-ETP R200 is the only one with a distinctive rolling skin, the same method was applied to correct the hardness of all other specimens. The difference before and after the correction proposed in Eq. 1 is represented in Fig. 10.

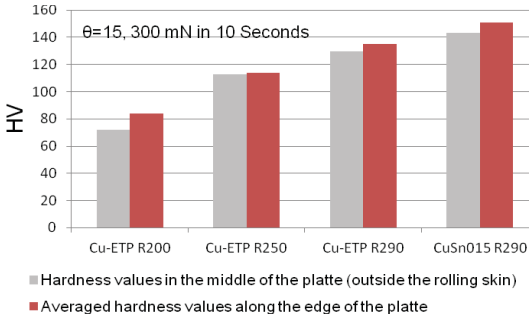

Fig. 10. Vickers Hardness of the four specimens after and before the adjustment suggested to consider the inhomogeneity of the plates due to the rolling skin

The difference that can be observed in Fig. 10 for the sample Cu-ETP R200 is due to the distinctive rolling skin. The difference observed for the rest of specimens is mainly caused by the measurement uncertainty.

Correlation of hardness values with material properties for implementation in a FEM code

Method 1: Scale factor for the $R_{p0,2\%}$ yield stress

Correlating a new $R_{p0,2\%}$ for each hardness value provides a description of the strain-hardened zone that can be easily implemented in a FEM code after an interpolation process. Each integration point of the FEM grid would got assigned different offsets of yield stress in order to take into account the strain-hardening caused by the stamping.

Fig. 11 shows the relationship between hardness and Rp0,2% for the four reference samples that was measured by means of the tensile tests.

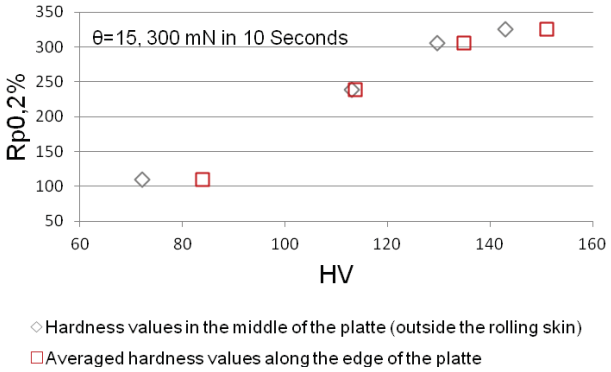

Fig. 11. Vickers Hardness vs. the $R_{p0,2\%}$ flow stress of the 4 reference samples

Method 2: Calculation of an initial plastic strain ε_{p0}

Each hardness value corresponds to a certain plastic strain. Knowing the relationship between these two parameters would be the second option to implement the effect of the strain hardening in the FEM Simulation of the cold joining process.

All integration points would get assigned the same flow curve, but an initial plastic hardening would be assigned to the elements affected by the hardening after the stamping process.

As already mentioned, several analytical approaches have been suggested to correlate a strain value to Vickers hardness. Nonetheless, explaining the value of the plastic strain with energy or similar approaches just guarantee an error below 20%.

A very simplified approach would be using the initial plastic strain values applied in Fig. 5b and correlating them to the Vickers hardness of each specimen (Fig. 12).

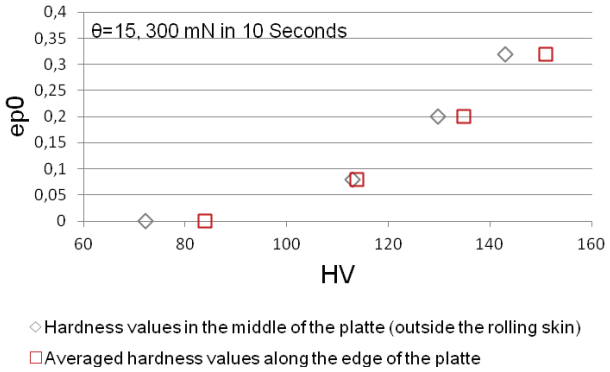

Fig. 12. Vickers Hardness vs. the εp0 flow stress of the 4 reference samples

4 DISCUSSION

Tensile tests and the true stress/ true strain constitutive behavior of the samples

The flow curve of polycrystalline copper shows three different ranges that are described in Fig. 13 [43-45].

The hardening exponent increases rapidly in the first stage due to the storage of dislocations. The onset cross slipping of screw dislocations produces a decrease of the hardening exponent on the second range. The third range shows a low constant hardening at high plastic strain.

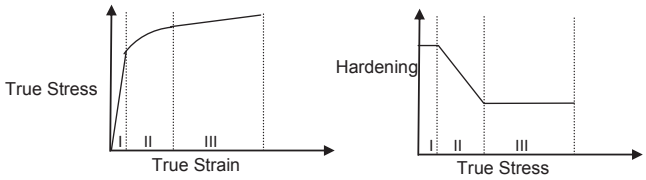

Fig. 13. Kocks-Meckig Plot. Polycrystalline deformation of f.c.c. materials

Due to their work-hardening, the flow curves of all four reference materials except Cu-ETP R200 show after the yield point a slow, constant hardening corresponding to

the third range. Thus the stress/ strain relation for the three hardest materials is linear after the yield point.

The relationship between the Vickers Hardness and the flow stress is directly proportional [6, 19, 22, 32, 48].

Therefore, not only the relationship between hardness and yield stress is linear for the Cu-ETP samples, but also the plastic strain can be linearly interpolated between the hardness values of Cu-ETP R250 and Cu-ETP R290.

Using the four different commercial plates for the validation of the method presents some limitations. The hardening mechanism between different samples and the hardening mechanisms during the stamping process are not the same due to the temperature treatment of the plates (Fig. 3). This effect of the made assumption is also visible in Fig. 5b, where it becomes evident that the samples are not just strain hardened specimens of the same flow curve.

Hardness measurements

The hardness screening of the strain-hardened areas show a significant effect of the stamping process as it was expected (Fig. 1) and confirms the need to reevaluate local material properties. Moreover, it gives additional information about the need of modeling the inhomogeneity due to the rolling skin of the plates, especially for the Cu-ETP R200 specimen.

Due to the linear relationship between HV and the flow stress, all samples except the CuSn015 alloy reveal, as expected, a linear H-$R_{0,2\%}$ correlation (the three Cu-ETP samples have a linear H- $R_{0,2\%}$ correlation with R^2>0,99). The $CuSn_{015}$ cannot be considered as a work hardened Cu-ETP sample, and cannot be taken into account in finding the correlation between the hardness and the flow properties.

The non homogeneity of the Cu-ETP R200 plate and the specimens for the tensile tests makes difficult to assign a single hardness value to the flow curve.

Interrupted uniaxial tensile test would provide more appropriate specimens to assess the hardness of a material with different plastic strains [51].

Implementation in the cold joining FEM Simulation

The linear correlation between HV and the flow stress makes the implementation of Method 1 in the cold joining process simulation very suitable, since a linear interpolation for the flow curve could be directly implemented between the bulk material and the most strain hardened point in the assembly part.

Furthermore, the constant hardening of the samples above certain hardness allows a linear interpolation for Method 2 too.

5 CONCLUSIONS

The first experiments to deliver new local material properties for the FEM simulation of the cold joining process showed the great potential of Vickers microindentation for the purpose.

The hardness screening of the stamped samples confirm that the local reassessment of the flow properties is absolutely necessary in the strain-hardened area and will not only make the FEM simulation of the cold joining much closer to reality but will imply a step forward on the designing and understanding of massive cold joining connectors.

The information about the anisotropy created by the stamping process gets lost if the reference samples with the known plastic strain are thermally treated and therefore show no anisotropic behavior. The experiments proved worthwhile a future manufacturing of specific samples that will allow finding an exact correlation between hardness and flow properties using interrupted tensile test. This would also make possible assessing the anisotropy of the material on the influence zone of the stamping.

A further optimization of the indentation system would also afford getting other information about the material, such as rate dependent behavior (Fig.4) or creep, with accessible indentation experiments in small volume specimens.

References

[1] T. Kanai, Y. Ando, S. Inagaki. Design of a Compliant Press-Fit Connection, IEEE Transactions on Components, Hybrids and Manufacturing Technology, 1985

[2] K. Wittig. Erfahrungen mit der Einpresstechnik für elektronischen Baugruppen in der Automotive-Anwendung, Systemintegration in der Mikroelektronik -SMT/HYBRID/ PACK., 2008

[3] R. Nolde. Einpresstechnik. Eine praxisnahe Einführung, Eugen G. Leuze Verlag, 1994

[4] J.P. Nobre, A. M. Dias, M. Kornmeier. An empirical methodology to estimate a local yield stress in work-hardened surface layers, Society for Experimental Mechanics, 2004

[5] J.Petruska, L. Janicek. On the evaluation of strain inhomogeneity by hardness measurement of formed products, Journal of Material Processing Technology, 2003

[6] F. O. Sonmez, A. Demir. Analytical relations between hardness and strain for cold formed parts, Journal of Materials Processing technology, 2007

[7] J. –H. Ahn. Effects of work-hardening characteristics on evaluating flow properties from indentation load-depth curve, Micromat Int. Conference, 2000

[8] R. M. Davies. The determination of static and dynamic yield stresses, Proceedings of the Royal Society of London, 1949

[9] S. Biwa, B. Storakers. An Analysis of fully plastic Brinell indentation, J. Mech. Phys. Solids Vol. 43 No. 8, 1995

[10] B. Taljat, T. Zacharia. New analytical procesure to determine stress-strain curve from spherical indentation data, Int. J. Solids Structures Vol. 35 No. 33, 1998

[11] N. Huber, E. Tyulyukovsky. A new loading history for identification of viscoplastic properties by spherical indentation, J. Mater. Res. Vol.19 No.1, 2004

[12] R. Hill, B. Storakers, A.B. Zdunek. A theoretical study of the Brinell hardness test, Proceedings of the Royal Society of London, 1980

[13] H. A. Francis. Phenomenological analysis of plastic spherical indentation, J. Eng. Mat. Technol., 1976
[14] M. M. Chaudhri. Strain hardening around spherical indentations, Phys. Stat. Sol 182, 2000
[15] J. -H. Ahn, D. Kwon. Derivation of plastic stress-strain relationship from ball indentations: Examination of strain definition and pileup effect, J. Mater. Res., 2001
[16] G. Sundarajan. Hardness- flow stress correlation in metallic materials, Bulletin of materials science, 1994
[17] D. Tabor. The Hardness and Strength of Metals, J. Inst. Met. 79, 1949
[18] G.M. Pharr, W.C. Oliver, F.R. Brotzen. On the generality of the relationship among contact stiffness, contact area, and elastic modulus during indentation, J. Mater. Res. Vol.7 No.3, 1992
[19] H. S. Chen, J. T. Krause, E. Coleman. Elastic constants, hardness and their implications to flow properties of metallic glasses, Journal of Non-Crystalline Solids, 1975
[20] M.Y. He, G. R. Odette, T. Yamamoto, D. Klingensmith. A universal relationship between indentation hardness and flow stress, Journal of Nuclear Materials 367-370, 2007
[21] W. J. Tomlinson. On the relation between hardness and the flow curve of metals, Journal of Material Science, 1968
[22] A. E. Tekkaya. Improved relationship between Vickers hardness and yield stress for cold formed materials, Steel Res. 304-310, 2001
[23] R. E. Lenhart. The relationship of hardness measurements to the tensile and compression flow curves, Wadc. Technical report 55-114, 1955
[24] K. Durst, M. Goeken, G. M. Pharr. Finite element simulation of spherical indentation in the elastic-plastic transition, Zeitschrift für Metallkunde, 2002
[25] Nayebi, R. El Abdi, O. Bartier, G. Mauvosin. New procedure to determine steel mechanical parameters from the spherical indentation technique, Mechanics of Materials 34, 2002
[26] G. Leyi, Z. Wie, Z. Jing, H. Songling. Mechanics analysis and simulation of material Brinell hardness measurement, Measurement 44, 2011
[27] Y. Chooi, J. H. Park, B. M. Kim, J. C. Choi, B. H. Min. Estimation of Relation between effective strain and Hardness by rigid-plastic FEM, Metals and Materials Vol. 6, 2000
[28] N. Guyot. Numerical Study of the Brinell test of elastoplastic indentation, ZAMM A. Angew. Math. Mech., 2000
[29] B. Backes, K. Durst, M. Goeken. Determination of plastic properties of polycrystalline metallic materials, Philosophical Magazine Vol. 86, 2006
[30] K. Durst, M. Goeken, H. Vehoff. Finite element study for nanoindentation measurements on two-phase materials, Journal of Materials Research, 2004
[31] A. C. Batista, J.P. Marinheiro, J. P. Nobre, A. M. Dias. Characterization of elastoplastic behavior using spherical indentation, Materials Science Forum, 2006
[32] A.E. Tekkaya. An improved relationship between Vickers hardness and yield stress for cold formed materials and its experimental verification, Annals of the CIRP Vol. 49, 2000
[33] M. Dao, N. Chollacopp, K. J. Van Vliet, T.A. Venkatesh, S. Suresh. Computational modeling of the forward and reverse problems in instrumented sharp indentation, Acta mater. 49, 2001
[34] A. K. Bhattacharya, W. D. Nix. Finite Element Simulation of indentation experiments, Int. J. Solids Structures Vol. 24, 1988
[35] R. Goodall. Investigation of the Constant load method for nanoindentation creep, Lecture Script University of Cambridge
[36] P. M. Sargent, M. F. Ashby. Indentation creep, Material science and Technology, 1992
[37] D. S. Stone, J. E. Jakes, J. Puthoff, A. A. Elmustafa. Analysis of indentation creep, J. Mater. Res. Vol. 25, 2012
[38] W. B. Li, J. L. Henshall, R. M. Hooper, K. E. Easterling. The mechanisms of indentation creep, Acta metal. Mater Vol. 39 No. 12, 1991
[39] K. Zhang, J. R. Weertman, J. A. Eastman. The influence of time, temperature and grain size on indentation creep in high-purity nanocrystalline and ultrafine grain copper, AIP Applied Physics Letters, 2012
[40] I.–C. Choi et al. Indentation creep revised, Journal of Material Research, 2012
[41] M. L. Oyen. Spherical indentation creep following ramp loading, Journal of Material Research, 2005

[42] B. N. Lucas, W. C. Oliver. Indentation power-law creep of high purity indium, Metallurgical and Materials Transactions Vol. 30A, 1999
[43] B. Mülders, Modellierung der Verfestigung technischer Aluminiumlegierungen, Dissertation RWTH Aachen, 2001
[44] H. Mecking, U. F. Kocks, Kinetics of flow and strain-hardening, Acta Metallurgica Vol. 29, 1981
[45] P.S. Follansbee, U. F. Kocks, A constitutive description of the deformation of copper based on the use of the mechanical threshold stress as an internal state variable, Acta Metallurgica Vol. 36, 1988
[46] W. Schmidt, Die Prüfkraftabhängigkeit der Vickershärte, Werkstatt und Betrieb, 1970
[47] D. Dengel, E. Kröske, Prüfkraftabhängigkeit der Vickershärte, HTM 39, 1934
[48] V. Läpple, Wärmebehandlung des Stahls,p.150-152, Europa Lehrmittel, 2010
[49] P. Maris, Stress and Strain distribution in Vickers indentation of coated materials, Advanced materials forum III, 2006
[50] A.E. Giannakopolus, Analysis of Vickers Indentation, Int. J. Solids Structures Vol.31 N. 19, 1994
[51] J.–Y. Kim, S.–K. Kang, J. R. Greer, D. Kwon, Evaluating plastic flow properties by characterizing indentation size effect using a sharp indenter, Acta Materialia Vol. 56, 2008

Influences of Toroidal Core Dimensions on Measured Properties of Magnetic Material

B. Koprivica and A. Milovanovic

[1] University of Kragujevac, Technical Faculty Cacak, Svetog Save 65, 32000 Cacak, Serbia

Abstract

In this paper we will present the analysis concerning influences of toroidal core dimensions on the measured results during testing magnetic materials. Nowadays, these influences have been analysed by several authors [1-6]. They analysed different influences of dimensions of toroidal core on the measured properties of magnetic materials. Mostly, variation of the specific losses with change of these geometric parameters has been analysed. Mainly, these authors concluded that inner diameter, outer diameter, strip width and core build-up has most impact on the results obtained. However, these conclusions are not clear enough when it concerned practical implementation. Aim of this paper is to, taking into account existing findings, further explain these influences. This can be useful in improving the mathematical models used for material characterization.

1 INTRODUCTION

Characterization of the ferromagnetic materials is very important because their wide applications. There are many measurements methods used for this purpose and one commonly used concerns the usage of wound toroidal core samples. These cores are often used in fabrication of current transformers and inductors. So, using them in material characterization is fully reasonable. In this, the magnetic hysteresis, the magnetization curve and the specific power losses have been mostly determined. These characteristics have been obtained through the measurement of the time representation, or average and effective value, of the magnetizing current and the secondary voltage. Using core parameters, effective length, cross-sectional area, number of turns of the primary and secondary windings and mass the magnetic field strength and induction can be calculated. Nowadays, time representation can be obtained successfully by using digital methods.

In this paper, presented results have been obtained by measurements by using virtual instrumentation based on PC with LabVIEW software [7]. Time representations of the magnetic field strength and magnetic induction have been measured. The magnetic hysteresis loop and magnetization curve have been obtained. All measured and calculated results have been saved on PC.

A number of measurements have been carried out on significant number of specimens. Tests have been done by using toroidal cores made of electrical steel having different dimensions. Measurements have been performed at frequency 50Hz, with

maximum magnetic field strength from 50 A/m to 1000 A/m. Variations of the results for different core geometry have been obtained during measurements.

2 MEASUREMENT METHOD

Applied measurement method is well known, commonly used by many investigators and engineers. This method has been previously used by authors for obtaining the magnetic hysteresis of ferromagnetic material [7]. The measurement setup has been presented in Fig. 1.

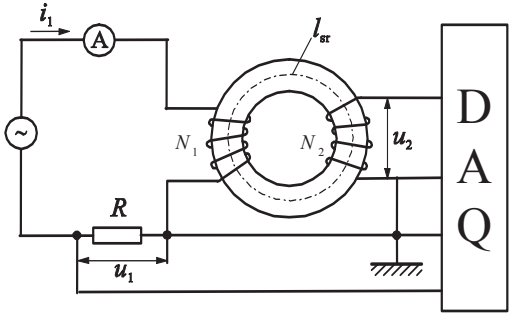

Fig 1: Measurement setup.

The magnetic field strength at which the measurements have been made can be calculated using the following relationship:

$$H(t) = \frac{N_1}{Rl_{sr}} u_1(t), \tag{1}$$

where N_1 is the number of turns of the magnetizing winding, $u_1(t)$ is the voltage at a time t across the resistor to determine the magnetization current, l_{sr} is the mean magnetic path length and R is the resistance of the resistor in series with the magnetizing winding.

The magnetic flux density can be calculated from the following equation:

$$B(t) = -\frac{1}{N_2 S}\int_0^t u_2(t)dt + K, \tag{2}$$

where N_2 is the number of turns of the secondary winding, $u_2(t)$ is the secondary voltage at a time t, S is the cross-sectional area of the test specimen and K is such that the time average of $B(t)$ is zero.

The magnetic hysteresis loop can be obtained by presenting $B(t)$ as function of $H(t)$. By successively increasing the magnetizing current, corresponding values of maximum magnetic field strength and maximum magnetic flux density can be obtained from which the magnetization curve can be plotted.

3 TEST SPECIMENS

The geometry of the test specimens and their actual dimensions have been presented in Fig. 2 and Table 1.

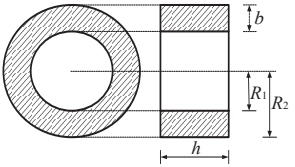

Fig 2: Test specimen geometry.

Table 1: Toroidal core samples dimensions.

I group						II group						
Coil	N_1	N_2	R_1 [mm]	R_2 [mm]	h [mm]	Coil	N_1	N_2	R_1 [mm]	R_2 [mm]	h [mm]	m [kg]
1	83	40	20	25	15	1	85	20	20	24	10	0.043
2	124	40	30	37.5	15	2	85	20	20	25	10	0.053
3	166	40	40	50	15	3	85	20	20	27	10	0.077
4	83	40	20	25	10	4	85	20	20	30	10	0.118
5	124	40	30	37.5	10	5	85	20	20	33	10	0.163
6	166	40	40	50	10	6	85	20	20	36	10	0.211
7	83	40	20	25	20	7	85	20	20	39	10	0.264
8	124	40	30	37.5	20	-	-	-	-	-	-	-
9	166	40	40	50	20	-	-	-	-	-	-	-

According to these dimensions the effective parameters of cores can be calculated as:

$$l_{sr} = (R_1 + R_2)\pi,\ S = (R_2 - R_1)h,\ S_m = \frac{m}{(R_1 + R_2)\rho\pi}, \tag{3}$$

where l_{sr} is the mean magnetic path length, S is the cross-sectional area, S_m is the cross-sectional area calculated by using the mass m and $\rho = 7.65\,\mathrm{gr/cm^3}$ is the material density.

Effective parameters of the test specimens have been presented in Table 2.

Table 2: Toroidal core effective parameters.

I group			II group			
Coil	l_{sr} [m]	$S\left[10^{-4}\mathrm{m}^2\right]$	Coil	l_{sr} [m]	$S\left[10^{-4}\mathrm{m}^2\right]$	$S_m\left[10^{-4}\mathrm{m}^2\right]$
1	0.1414	0.750	1	0.1382	0.4	0.4066
2	0.2121	1.125	2	0.1414	0.5	0.49
3	0.2827	1.500	3	0.1476	0.7	0.6817
4	0.1414	0.500	4	0.1571	1.0	0.982
5	0.2121	0.750	5	0.1665	1.3	1.2797
6	0.2827	1.000	6	0.1759	1.6	1.5678
7	0.1414	1.000	7	0.1853	1.9	1.8618
8	0.2121	1.500	-	-	-	-
9	0.2827	2.000	-	-	-	-

The first group of the specimens has been made of material with known magnetization characteristics given by manufacturer. Dimensions of the cores have been cho-

sen such to satisfy two conditions: the ratio of the inner to outer radius should be at least 0.8 (the variation of the magnetic field strength and induction from outer to inner edge of the specimen should be small) and the quotient of the number of turns of the magnetizing winding N_1 and the mean magnetic path length l_{sr} should be constant (the same magnetizing current should produce the same magnetic field strength in all specimens in the first group).

The second group of the specimens have been made of material with unknown magnetization characteristics. Dimensions of the cores have been chosen as in [1,2] with intention of producing the comparable results. In [1,2] the aspect ration and the winding ratio of the specimen have been defined as $AR = h/b$ and $WR = R_1/h$, respectively, where h is the strip width and b is the wound thickness bild-up of the toroidal core. So, dimensions of the cores have been chosen such that the strip width is constant, the inner radius is constant and the outer radius is variable (WR is constant and AR is variable). This has been done in this way because the conclusions from [1,2] were such that it can be said that effect of AR on the measured results is much simpler for analysis then the effect of WR.

Aspect and winding ratios of the test specimens have been presented in Table 3.

Table 3: Aspect and winding ratios.

I group			II group		
Coil	AR	WR	Coil	AR	WR
1	3	1.33	1	2.5	2
2	2	2	2	2	2
3	1.5	2.66	3	1.43	2
4	2	2	4	1	2
5	1.33	3	5	0.77	2
6	1	4	6	0.625	2
7	4	1	7	0.53	2
8	2.66	1.5	-	-	-
9	2	2	-	-	-

4 RESULTS

Fig. 3 shows the variation in the magnetic hysteresis for specimens in the first group when the magnetic field strength is 100A/m (the first row) and 300A/m. Each graph in this figure shows three hysteresis loops for specimens with same inner and outer radius but with different strip width.

The variations of the magnetization curves for specimens in the first group, along with known ThyssenK PowerCore C 130-27 magnetization curve, have been presented in Fig. 4. Deviations of the measured magnetic induction has been calculated as $\delta[\%] = 100(B - B_m)/B$, where B is the magnetic induction given by manufacturer and B_m is the measured magnetic induction. Obtained results have been presented in Table 4.

From Fig. 4 and Table 4 it can be seen that magnetization curve of Coils 7, 8 and 9 have almost the same shape as one given from manufacturer and the deviation of the results is within few percent. Other magnetization curves have much greater deviation and their shape is deformed. In [1,2] this has been explained in this way. Higher AR gives fewer losses and higher WR gives higher losses. Also, WR can be dominated by the effect of strip width in that way that the loss depends on h as $200/h$. So, increase of losses with increase of WR can be decreased by using wider strip width. All specimens in the first group have significant AR which gives less losses and have significant WR which gives higher losses. But, Coils 7, 8 and 9 have significant strip width which gives less losses. This is the reason why the best results have been obtained with these three coils. And more, the best result has been obtained with Coil 9 which has wide strip width and medium AR and WR.

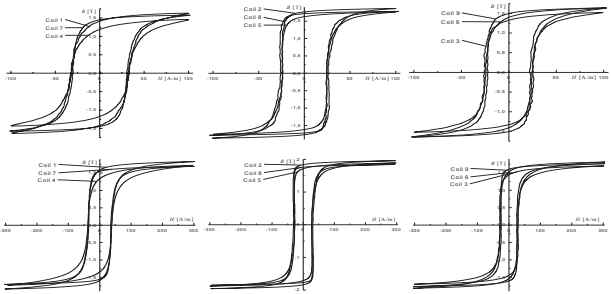

Fig 3: Variation in the hysteresis.

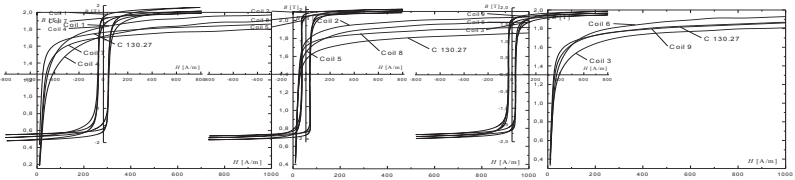

Fig 4: Variation in the magnetization curves.

Table 4: Deviations of the magnetic induction.

$H[\mathrm{A/m}]$	$\delta[\%]$								
	Coil 1	Coil 2	Coil 3	Coil 4	Coil 5	Coil 6	Coil 7	Coil 8	Coil 9
50	12.26	-14.19	12.91	23.87	-6.45	6.45	8.39	-10.96	2.58
100	1.21	-12.64	7.84	12.05	-6.62	0.01	4.22	-7.82	0.61
200	-2.87	-12.12	4.64	4.64	-8.08	-2.87	2.90	-5.76	-0.56
300	-4.52	-11.34	2.86	1.72	-7.93	-3.39	2.86	-5.09	-0.55
400	-5.59	-11.20	2.27	0.03	-7.83	-3.90	2.84	-5.03	-1.09
500	-6.04	-10.46	2.80	-1.07	-7.14	-3.83	3.35	-3.83	-0.52
600	-5.45	-10.39	2.79	-0.51	-7.65	-3.80	2.79	-4.35	-0.51
700	-6.51	-9.78	2.78	-2.14	-7.05	-4.87	3.32	-3.77	-0.50
800	-6.46	-10.26	2.23	-2.66	-7.55	-3.75	3.31	-3.75	-0.49
900	-6.17	-9.96	2.50	-1.83	-7.25	-4.00	2.50	-4.00	-0.75
1000	-6.41	-10.19	2.23	-3.17	-6.95	-4.25	2.77	-3.71	-1.01

From the previous analysis it can be concluded that the effects of specimen dimensions are very complex. So, for better understanding of individual effects the second group of specimens with constant WR and variable AR has been made. The magnetic hysteresis loops and the magnetization curves obtained by measurements have been presented in Fig. 5. It can be seen that the differences between these loops and curves are very small (except for Coil 5, but this variation is within several percents). According to these results it can be concluded that the effect of AR is not significant.

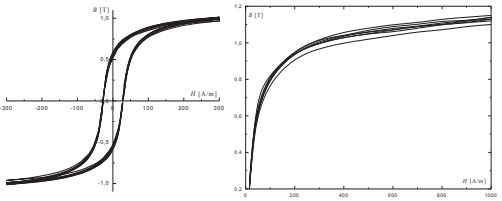

Fig 5: Variation of the hysteresis loops and magnetization curves.

5 CONCLUSIONS

Effects of the dimensions of toroidal core specimen used for characterization of the ferromagnetic material to the measured results are evident. Some remarks in this area have been obtained in earlier research by several authors [1-6]. But, obtained conclusions were complicated for practical implementation. In this paper this matter has been further investigated and some interesting results have been obtained. The magnetization curves and hysteresis loops of the specimens have been measured and presented in this paper. The variations between results obtained have been discussed to explain the effects of AR, WR and strip width. Furthermore, just effect of AR has been investigated. The results obtained show that in this case this effect is not significant as it has been previously stated in [1,2]. There may be many reasons for this but one most relevant may be the measurement method. Nowadays, the digital measurement method based on PC can be performed with high accuracy and precision. So, it can be concluded that this matter should be investigated more to explain individual effects when digital measurement method has been used. This will be matter of further investigations by these authors.

Acknowledgements

This paper has been supported by Scientific Project TR 33016 financed by Ministry of Education and Science of the Republic of Serbia.

References

[1] A.J. Moses, P.C.Y. Ling. Dimensional Factors Affecting Magnetic Properties of Wound Cores, Physica Scripta **40** (1989) 249-251.

[2] W. Grimmond, A.J. Moses, P.C.Y. Ling. Geometrical Factors Affecting Magnetic Properties of Wound Toroidal Cores, IEEE Transaction on Magnetics **25** (1989) 2686-2693.

[3] K. Saitoh, K. Shinya, E. Miyazawa. Influence of Dimension Ratio and Magnetizing Conditions on the AC Magnetic Properties of Tape-wound Ring Core, Electrical Engineering in Japan **129** (1999) 1-8.

[4] K. Saitoh, K. Shinya, E. Miyazawa. Effect of Dimension Ratio on the Magnetic Properties of Tape-wound Toroidal Core with AC Excitation, Electrical Engineering in Japan **113** (1993) 9-16.

[5] P. Nakmahachalasint, K.D.T. Ngo, L. Vu-Quoc. Effective Magnetic Parameters in the Presence of Hysteresis, IEEE Transaction on Aerospace and Electronic Systems **40** (2004) 1100-1104.

[6] P. Nakmahachalasint, K.D.T. Ngo, L. Vu-Quoc. Effective Parameters for Toroidal Cores based on Nonlinear Magnetization, IEEE Transaction on Magnetics **41** (2005) 2432-2435.

[7] B. Koprivica, A. Milovanovic, M. Djekic. Determination of Characteristics of Ferromagnetic Material using Modern Data Acquisition System, Serbian Journal of Electrical Engineering **6** (2009) 451-459.

Carbon nanotubes - properties and applications

Mário Kotlár[1], Viliam Vretenár[2], Marian Veselý[1], Róbert Redhammer[1], Peter Schaaf[3]

[1] Institute of Electronics and Photonics, Slovak University of Technology, Ilkovičova 3, 812 19 Bratislava, Slovakia
[2] Danubia NanoTech, s.r.o., Ilkovičova 3, 841 04 Bratislava, Slovakia
[3] Ilmenau University of Technology, Institute of Materials Engineering, Gustav-Kirchhoff-Strasse 5, 98693 Ilmenau, Germany

Abstract

Carbon nanotubes offer excellent electrical, mechanical and thermal properties. We can use them in many applications ranging from transistors to composite materials. In our experiments carbon nanotubes were synthesized by using the chemical vapor deposition, arc discharge and laser ablation technologies. By proper choice of experimental conditions single walled carbon nanotubes (SWCNTs) with different morphology have been successfully produced. To illustrate properties and possible applications of carbon nanotubes we prepare "buckypapers" - bulk material consisting only from pure SWCNTs and single-walled carbon nanotubes that conductively connect metal electrodes directly in their growth by chemical vapor deposition.

1 INTRODUCTION

Carbon nanotube is a cylindrically shaped structure which was discovered in 1991 by Iijima [1]. Carbon atoms are arranged in a hexagonal crystal lattice (Fig. 1). We can consider carbon nanotube as one graphite layer that is rolled up into cylinder having diameter and length in the order of nanometers and micrometers, respectively. Carbon nanotubes were classified into two kinds: single-wall carbon nanotubes and multi-wall carbon nanotubes. We can describe carbon nanotube by chiral vector and chiral angle, or by pair of integers:

$$C_h = n\mathbf{a}_1 + m\mathbf{a}_2 \equiv (m,n) \tag{1}$$

$$\theta = \tan^{-1}\left[\sqrt{3}m/(m+2n)\right] \tag{2}$$

Chiral angle is angle between chiral vector C_h and unit vector $\mathbf{a}_1$. For different chiral angle we can describe three basic types of carbon nanotubes. The chiral angle for the axis of so called *zigzag* carbon nanotube corresponds to $\theta = 0^\circ$, for *armchair* carbon nanotube corresponds to $\theta = 30^\circ$ and for *chiral* carbon nanotube corresponds to $0<\theta < 30^\circ$ [2]. Carbon nanotube diameter d_t can be written as:

$$d_t = C_h/\pi = \sqrt{3}a_{CC}\left(m^2 + mn + n^2\right)^{1/2}/\pi \tag{3}$$

where a_{CC} is nearest neighbor C-C distance (1.421 Å) and *m, n* are integers.
If we want to calculate electronic structure of carbon nanotubes we have to start by considering the electronic structure of graphene with periodic boundary conditions in

circumference direction - only discreet number of wavelengths can fit around the tube diameter. Therefore electronic structure of carbon nanotubes depends only on the diameter of carbon nanotube and chirality of hexagonal crystal lattice. According to their electronic properties they are semiconducting or metallic. Two-thirds of nanotubes are semiconducting and one-third is metallic. Thanks to their structure and electronic properties metal nanotubes act like 1D metal – quantum wire [3], [4]. Carbon nanotubes are characteristic with ballistic transport of electrons and conductance of SWCNT is $G_0 = 4e^2/h \approx 155$ μS.

Carbon nanotubes can be produced by several methods: arc discharge (AD), chemical vapor deposition (CVD) and laser ablation (LA). Chemical vapor deposition is the simplest and probably the most widely used technology for their growth, but arc discharge and laser ablation produce carbon nanotubes of superior quality. Product is characterized mainly by electron microscopy (SEM, TEM), thermogravimetric analysis (TGA) and Raman spectroscopy. Due to their unique structure carbon nanotubes (CNTs) have many interesting electronic, mechanical and chemical properties. They can be used in transistors [5], memory elements [6], nanomechanical mass sensors [7], transparent conductive layers and they can replace metal conductors etc. But currently there is no method for precisely manipulating and positioning individual carbon nanotubes and every growth technique produces carbon nanotubes with different chiralities and diameter (different electronic properties).

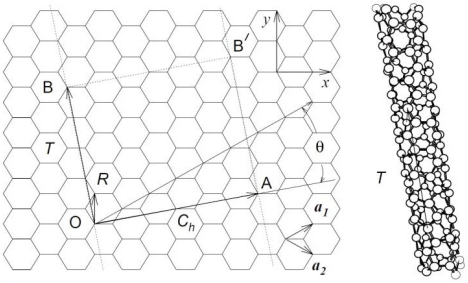

Fig. 1. Hexagonal crystal lattice of carbon nanotubes. One can describe carbon nanotube by chiral vector C_h and chiral angle θ.

2 BUCKYPAPERS - POSSIBLE ALTERNATIVE TO METAL CONDUCTORS

Carbon nanotubes thanks to the van der Waals forces tend to stick together and create ropes consisting from large number of carbon nanotubes. By using proper surfactant (NMP or SDS) and sonification we can separate them and create disperse suspension of carbon nanotubes. After filtration of this suspension carbon nanotubes were collected on a filter forming a thin film disk of pure nanotubes - buckypaper. For this purpose we can produce carbon nanotubes by arc discharge and laser ablation. In arc discharge technology we are using pair of graphite electrodes - cathode and anode. Arc discharge is ignited by short contact between electrodes in an inert atmosphere (He) with pressure of 10 – 80 kPa. Incoming electrons transfer their energy to the anode which causes material to sublime. This means that anode is consumed in the process. According to anode composition multi-walled carbon nano-

tubes (pure graphite anode) and single-walled carbon nanotubes (anode consists from graphite and metal catalysts) are grown. In our experiments we are using anode of composition G/Ni/Y (95/4/1 at. %) or G/Fe/Ni (96.4/1.8/1.8 at. %). In laser ablation technique laser in continual or pulsed regime is used to vaporize graphite target. Graphite target consists of graphite and catalytic metals mostly bimetal for example Ni/Co [8]. Apparatus consists of furnace, quartz tube, Cu water cooled collector. Graphite target is evaporated by laser in the flow of Ar or He. Carbon nanotubes in the flow of gas are deposited on the cold copper collector. SWCNTs were found typically grouped together by van der Waals forces over most of their length. Product has „web" like structure and typically consist of single walled carbon nanotubes and impurities in form of graphite particles, metal catalyst, amorphous carbon etc. In our experiments SWCNTs were prepared by laser ablation method at total gas pressure of 61.5 kPa in Ar atmosphere and at temperature of about 1 160 °C. Used target consists of 98 wt. % of graphite, 1 wt. % of Ni and 1 wt. % of Co.

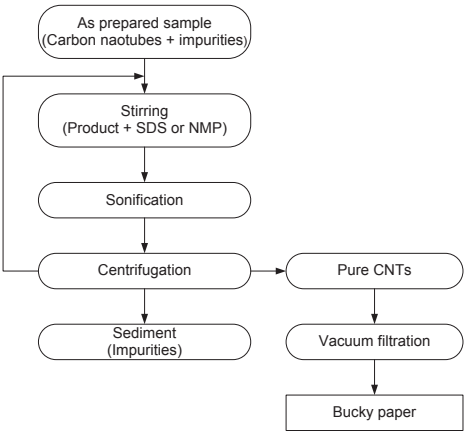

Fig. 2. Purification of carbon nanotubes by physical methods and production of buckypapers.

Before application of carbon nanotubes it is very important to clean the product from impurities. Purification methods of CNTs can be basically classified into three categories: chemical, physical and the combination of both. In our experiments we are using physical methods. Physical methods are based on sonification, centrifugation and filtration. Centrifugation is related to the effect of the gravity on particles in suspension (i.e. two particles of different masses settle in a tube at different rates in response to gravity). Commonly, the buckypapers (30 - 50 μm thin porous structures) are produced from pure SWCNTs by vacuum filtration (Fig. 2). The measured conductivity (four probe method) is in the range from 500 to 1000 Scm^{-1} which is much lower than that of individual CNTs, of 10 000 – 30 000 Scm^{-1} [9] and metals. This is caused mainly by short length, poor alignment and high contact resistance. Main goal is to get these properties to buckypapers or other composite materials. One possibility is chemical functionalization by adding active species to nanotube surface (for example by using of HNO_3). Big advantage of buckypaper is light weight - much lower than for metals.

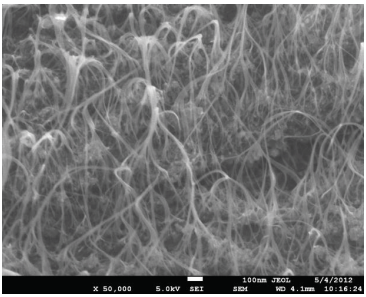

a)

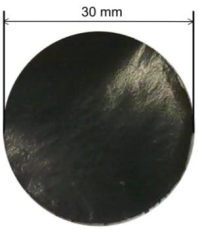

b)

Fig. 3. a) Cross section SEM image and b) Optical image of the Buckypaper 30 mm in diameter.

3 CONNECTING CARBON NANOTUBES WITH METAL ELECTRODES

There exist several methods for connecting carbon nanotubes with metal electrodes. The most frequently used is a deposition from a droplet of dispersed solution containing SWNTs [10–12]. Carbon nanotubes are produced by a laser ablation or an arc discharge method. Synthesis is then followed by cleaning of carbon nanotubes. After solvent evaporation carbon nanotubes lay on the electrodes. Disadvantage of this is high contact resistance between CNTs and electrodes [13]. The second widely used method is dielectrophoresis [14], [15]. In this method an electric field is applied across electrodes for achieving deposition of carbon nanotube from a solution. This method can be used for large distances between electrodes (more than 500 μm) and for large density of carbon nanotubes. The third method is a Direct CVD method [5], [16], [17]. Carbon nanotubes are directly synthesized on the top of the electrodes from the metal catalysts. This method is based on the fact that carbon nanotubes grow between metal nanoparticles and conductively connect them.

In our experiments first a 3 mm by 3 mm Cr/Cu interdigitated electrodes were deposited on the top of the SiO_2 by using photolithography and lift-off. Then Al/Ni (10/1 nm) two-layered films were evaporated as a catalyst layer to the surface of electrodes and then the resist was removed. Carbon nanotubes were grown by chemical vapor deposition. Experiments were carried out in a tube furnace with quartz tube with inner diameter of 40 mm in atmospheric pressure. Methane (CH_4) was used as a source of hydrocarbons. The temperature of the furnace was ramped up to 1 000 °C and stabilized. After that the samples were moved into the furnace and annealed in the flow of Ar/H_2 mixture for 10 min. The growth of carbon nanotubes was performed then in the flow of $Ar/H_2/CH_4$ mixture for 10 min. Both processes (annealing and growth) were run at the same temperature - 850 °C. After CNTs growth, the samples were moved out from the furnace center and the quartz tube was continuously purged with flow of Ar until the temperature has reached 90 °C. The structural morphologies of synthesized CNTs were characterized by scanning electron microscopy. Distance between the electrodes is around 2 μm. As carbon nanotubes grow they overcome gap between electrodes and connect with catalyst particles in the opposite electrode. One of the possible explanations of this fact is that carbon nanotubes grow in random direction but thanks to high temperature vibrations they continue to grow until they reach opposite electrode. Thanks to these phenomena they are able to make conductive connection between two electrodes. Measured conductance between electrodes de-

pends on the density of carbon nanotubes bridging metal electrodes. In Fig. 4, the measured VA characteristic for the typical sample with low density of carbon nanotubes is displayed.

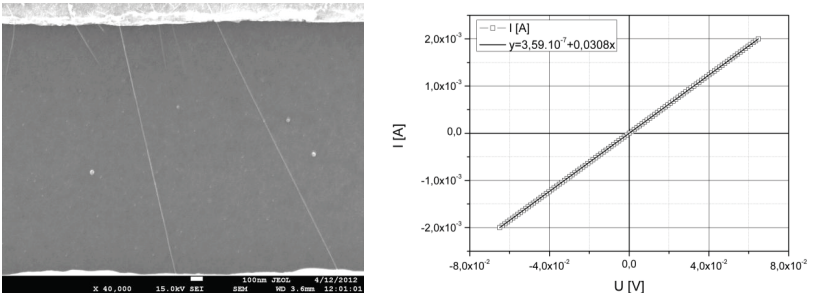

a) b)

Fig. 4. a) Single-walled carbon nanotubes bridging metal electrodes and b) Measured conductance of a typical sample.

4 CONCLUSIONS

Carbon nanotubes combine interesting electronic and thermal properties together with high mechanical resistance. In two examples we illustrate possible applications of carbon nanotubes. Carbon nanotube buckypaper can replace metal conductors. Big advantage of this material is low weight and high thermal conductance, but electrical conductance is still low for practical applications. The second application is a direct growth of carbon nanotubes between metal electrodes. This structure can be used as chemical sensor. With this method it is possible to grow individual carbon nanotube between metal contacts – applications are for example transistors, memory elements or nanomechanical mass sensors.

Acknowledgements

This work was financially supported by grant of Slovak Research and Development Agency No. APVV-0548-07 and Ministry of Education of Slovak Republic and the Slovak Academy of Sciences No. VEGA-1/1102/11 and 1/1103/11 and DAAD project 507 552 00.

References

[1] S. Iijima, “Helical microtubules of graphitic carbon,” *Nature*, vol. 354, no. 6348, pp. 56-58, Nov. 1991.

[2] M. S. Dresselhaus, G. Dresselhaus, R. Saito, and A. Jorio, “Raman spectroscopy of carbon nanotubes,” *Physics Reports*, vol. 409, no. 2, pp. 47-99, Mar. 2005.

[3] R. Saito, M. Fujita, G. Dresselhaus, and M. Dresselhaus, “Electronic structure of graphene tubules based on C60,” *Physical Review B*, vol. 46, no. 3, pp. 1804-1811, Jul. 1992.

[4] C. Dekker, “Carbon Nanotubes as Molecular Quantum Wires,” *Physics Today*, vol. 52, no. 5, p. 22, 1999.

[5] M. Muoth, T. Helbling, L. Durrer, S.-W. Lee, C. Roman, and C. Hierold, “Hysteresis-free operation of suspended carbon nanotube transistors.,” *Nature nanotechnology*, vol. 5, no. 8, pp. 589-92, Aug. 2010.

[6] G. E. Begtrup, W. Gannett, T. D. Yuzvinsky, V. H. Crespi, and A. Zettl, “Nanoscale Reversible Mass Transport for Archival Memory,” vol. 9, no. April, pp. 1835-1838, 2009.

[7] J. Chaste, A. Eichler, J. Moser, G. Ceballos, R. Rurali, and A. Bachtold, “A nanomechanical mass sensor with yoctogram resolution.,” *Nature nanotechnology*, Apr. 2012.

[8] T. Guo, P. Nikolaev, A. Thess, D. Colbert, and R. Smalley, “Catalytic growth of single-walled manotubes by laser vaporization,” *Chemical Physics Letters*, vol. 243, no. 1–2, pp. 49-54, Sep. 1995.

[9] I.-W. P. Chen, R. Liang, H. Zhao, B. Wang, and C. Zhang, “Highly conductive carbon nanotube buckypapers with improved doping stability via conjugational cross-linking.,” *Nanotechnology*, vol. 22, no. 48, p. 485708, Dec. 2011.

[10] M. Rinkiö et al., “High-yield of memory elements from carbon nanotube field-effect transistors with atomic layer deposited gate dielectric,” *New Journal of Physics*, vol. 10, no. 10, p. 103019, Oct. 2008.

[11] Y.-M. Lin, J. Appenzeller, J. Knoch, and P. Avouris, “High-Performance Carbon Nanotube Field-Effect Transistor With Tunable Polarities,” *IEEE Transactions On Nanotechnology*, vol. 4, no. 5, pp. 481-489, Sep. 2005.

[12] H. B. Peng et al., “Patterned growth of single-walled carbon nanotube arrays from a vapor-deposited Fe catalyst,” *Applied Physics Letters*, vol. 83, no. 20, p. 4238, 2003.

[13] C. Chen et al., “A method for creating reliable and low-resistance contacts between carbon nanotubes and microelectrodes,” *Carbon*, vol. 45, no. 2, pp. 436-442, Feb. 2007.

[14] A. Subramanian and L. Dong, “Assembly of arrays of individual lateral nanotube emitters on nanoelectrodes,” *, 2005. 5th IEEE*, no. July, 2005.

[15] J. Wu, “A MEMS-based ionization gas sensor using carbon nanotubes and dielectric barrier,” in *2008 3rd IEEE International Conference on Nano/Micro Engineered and Molecular Systems*, 2008, pp. 824-827.

[16] W. Xiong et al., “Controlled-growth of single-walled carbon nanotubes using optical near-field effects,” *Proceedings of SPIE*, vol. 7202, no. 402, pp. 720209-720209-8, 2009.

[17] J. Shi et al., “Direct synthesis of single-walled carbon nanotubes bridging metal electrodes by laser-assisted chemical vapor deposition,” *Applied Physics Letters*, vol. 89, no. 8, p. 083105, 2006.

Boron doped diamond for trace metal detection

Pavol Michniak[1], Marian Vojs[1], Miroslav Behul[1], Marian Veselý[1], Vladimír Tvarožek[1], Andrej Vincze[2], Marcus Wilke[3], Thomas Kups[3], Diana Rossberg[3], Peter Schaaf[3]

[1] Institute of Electronics and Photonics, Slovak University of Technology, Ilkovičova 3, 812 19 Bratislava, Slovak Republic

[2] International Laser Centre, Ilkovičova 3, 841 04 Bratislava, Slovak Republic

[3] Ilmenau University of Technology, Institute of Materials Engineering, Chair Materials for Electronics, Gustav-Kirchhoff-Strasse 5, 98693 Ilmenau, Germany

Abstract

In recent days the synthetically grown diamond layers are very progressive materials for various fields of applications. Diamond thin films were prepared by Hot Filament Chemical Vapour Deposition (HF CVD) method [1]. During the deposition in the reactor trimethylboron (TMB) is present as doping gas, boron doped diamond (BDD) can be produced. In this contribution BDD layers were analysed, identically grown with different B/C ratio in gas phase. However, mercury toxicity, future regulations and occupational health considerations may severely restrict the use of mercury (MFE). In search for alternative electrode materials, bismuth-film electrodes (BiFE) offer comparable performance to MFE for anodic stripping voltammetry measurements of trace metals, as it was shown [2]. The resulting BDD electrodes were analysed using Scanning Electron Microscopy (SEM), Raman spectroscopy and Glow Discharge Optical Emission Spectroscopy (GDOES) to determine sample properties. Electrochemical measurements were done by square-wave voltammetry and Zn, Cd, Pb were detected. During SWASV experiments in Pb(II), Cd(II) and Zn(II) solutions well-shaped stripping peaks were obtained whose heights varied linearly with analyte concentration in the range from 1×10^{-8} to 10^{-7} M, both in acetate buffer 4 – 5 pH. Under optimal conditions detection limits of 4.82×10^{-9}, 2.06×10^{-9} and 2.58×10^{-9} M were achieved for Pb(II), Cd(II) and Zn(II) with RSD (n=100) of 11.95 %, 4.83 % and 26.75 %, respectively.

1 INTRODUCTION

The recent development of material deposition methods leads also to thin diamond film production on various substrates. The technologies used for the diamond thin film formation are based on chemical vapour deposition (CVD) [1]. Diamond thin films are very useful for many applications, now they are used also in electrochemistry. Detection of trace metals is used to monitor pollution in environment. Previously used mercury-film electrodes (MFE) caused pollution in addition [3]. Without trace metal detection, BDD electrodes are used to detect dopamine, ascorbic acid and uric acid by cyclic voltammetry, as well as other chemical elements and compounds [4]. In the

future it is expected to fabricate microelectronic systems based on principle of Square Wave stripping voltammetry (SWASV) [5].

The grown diamond layers can be analysed using analytical methods to specify their properties. They inform about surface morphology, crystalline structure or chemical composition of grown thin films. The surface morphology is studied with Scanning Electron Microscopy (SEM). Raman Spectroscopy was used as a non-destructive technique to detect carbon phases and the boron concentration of diamond thin films [1]. Glow Discharge Optical Emission Spectroscopy (GDOES) provides rapid analysis of the atomic composition of thin films, which are sputtered by exposing them to Ar plasma and then characteristic photon spectra excited by sputtered atoms are observed [6].

2 EXPERIMENTAL DETAILS

The diamond thin films were prepared by Hot Filament CVD (HF CVD). The nucleation process was initiated using diamond powder in ultrasonic bath in demineralized water after 15 minutes. Diamond thin films were prepared on thermal SiO_2 300 nm thick layer, which was prepared on Si substrate.

The Chemical Vapour Deposition (CVD) involves a gas phase chemical reaction occurring above a solid surface, which causes deposition onto that surface. The most popular method for the growth of diamond thin films under low pressures is HF CVD. 5 pcs of hot filaments are used in our set up. Tungsten (after carbonation process tungsten carbide) filaments are heated up to 2,000 °C to activate the H_2 and CH_4 gases. A diamond film is then deposited onto a substrate, which is located about 10 mm under the filaments on a molybdenum holder. The pressure in the chamber is kept at 3 kPa and rotary pump is used for chamber evacuation. Before starting the growth process, the substrate surface must be prepared for the growth. This step is described as a diamond seeding process or also nucleation [7]. Substrates were 15 min sonicated in deionized water with 3-5 nm diamond powder (Sigma Aldrich). Substrate temperature was kept in the range from 650 °C to 700 °C and the deposition time was 120 minutes. Samples were prepared at different TMB (Trimethylboron) gas flows, which is a source for B and B/C gas ratio is a ratio of TMB to CH_4 (ppm).

GDOES measurements were done after deposition and boron concentration in diamond thin layer was determined as an average from a large number of values from BDD layer depth profile [6] (tab. 1).

3 RESULTS

SEM image of sample shows a cross section. Surfaces are homogenously evenly covered with a diamond structure. A significant difference between samples is not observed. The Fig.1 shows SEM picture of sample with B/C ratio of 10,000 ppm.

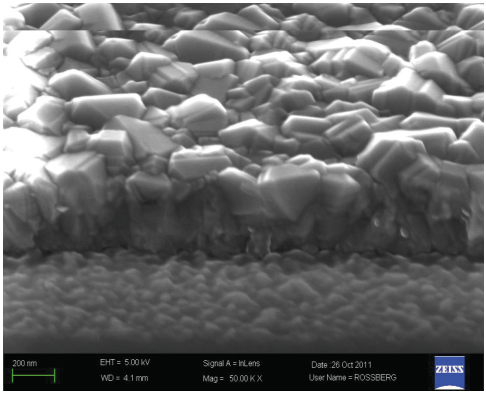

Fig 1: SEM Picture of sample BDD layer with B/C ratio of 10 000 ppm

The Fig. 2 shows the Raman spectra, which were obtained at room temperature using a He-Ne laser with wavelength of 632 nm. The diamond peak centred at 1 333 cm^{-1} decreases with an increased B/C ratio. Raman broad bands centred at 500 cm^{-1} and 1 225 cm^{-1} are visible only for high boron concentration. Peaks at 520 cm^{-1} and 925 cm^{-1} are characteristic for Silicon. For high boron concentration the peak at 1 580 cm^{-1} characteristic for micro-graphite is not visible [8].

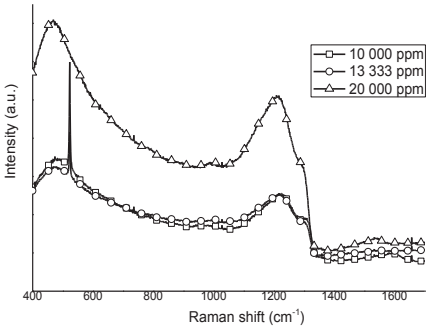

Fig 2: Raman spectra of BDD (B/C): a) 10 000 ppm, b) 15 000 ppm, c) 20 000 ppm

For voltametric measurements three-electrode arrangement was used, Ag/AgCl as a reference electrode and platinum plate as a counter electrode. Voltammetric measurement was performed with an electrochemical potentiostat/galvaniostat PGSTAT128N from METROOHM AUTOLAB COMPANY. Trace metals were presented in 0.1 mol/l HNO_3. Acetate buffer with pH=4, 4.5 and 5 were used in experiment. Before each measurement the electrode was cleaned by 30 cycles in acetate by Cyclic Voltammetry (CV) between -1.5 – +1.5V.

Measurements were done in a range from -1.75 to +0.5 V. Measurement with acetate without Bismuth and trace metals was done at first. Next bismuth to c (Bi) =1.10^{-6} mol/l and metals (Pb, Cd, Zn) from c (Me) = 10 to 100.10^{-9} mol/l with step 1.10^{-8} mol/l. In Fig. 3 peaks for Zn at potential of about -1.25 V, Cd at -0.8 V and Pb at -0.6 V are visible. Peak at -0.2 V is characteristic for Bi [2].

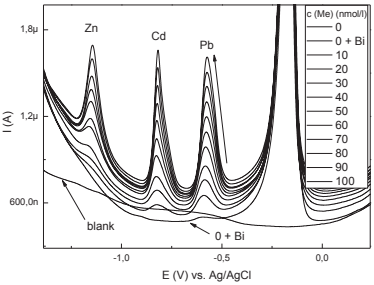

Fig 3: Square wave stripping voltammograms of BDDE 10 000 ppb B/C (E_{step} = 5 mV, E_{pulse} = 50 mV and frequency 100 Hz). Dependence of current responses of BDDE on concentration of target metals in 0.1 mol/l acetate buffer (pH 5); preconcentrated at −1.4 V for 120 s; concentration of Bi(III):

Measurements were done for solution with different pH. In Fig. 4 SWASV with c (Me) = 10^{-7} mol/l and c (Bi) = 10^{-6} mol/l for different pH (4, 4.5 and 5) of 0.1 mol/l acetate buffer is shown.

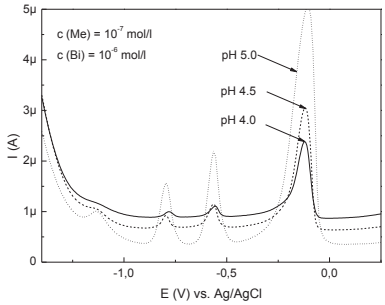

Fig 4: SWASV of BDDE 10 000 ppb B/C: (E_{step} = 5 mV, E_{pulse} = 50 mV and frequency 100 Hz). Dependence of current responses of BDDE on pH 0.1 mol/l acetate buffer with target metals c(Me)=10^{-7}mol/l,; preconcentrated at −1.4 V for 120 s; concentration of Bi(III): 1.10^{-6} mol/l.

Measurement at pH= 5 were done on BDD electrodes with B/C ratio of 10 000 ppm, 13 000 ppm and 20 000 ppm and linearity R^2, Limit Of Detection (LOD 3xSD/slope) and Sensitivity (S) were calculated (Tab. 1) from SWASV. LOD is best for electrode with B/C of 10 000 ppm and it rises with increased B/C ratio (Fig. 5).

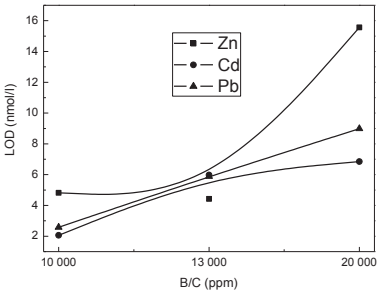

Fig 5: Dependence of LOD as influenced by B/C ratio of BDD

4 CONCLUSIONS

In Table 1 linearity R^2, Limit Of Detection (LOD) and sensitivity (S) for metals Zn, Cd and Pb for electrodes with B/C 20 000 ppm, 13 000 ppm and 10 000 ppm are shown. The best value for LOD is 2.06 nmol/l, for Cd on electrode B/C 10 000 ppm, that is also the best electrode for LOD of Pb (2.58 nmol/l). LOD for Zn is the best value of 4.42 for electrode B/C with 13 333 ppm. Relative standard deviation (RSD) was calculated for 100 repetitive measurements.

Tab. 1:

	20 000 ppm B/C			**13 333 ppm B/C**			**10 000 ppm B/C**		
	Zn	**Cd**	**Pb**	**Zn**	**Cd**	**Pb**	**Zn**	**Cd**	**Pb**
R^2	0.973	0.996	0.992	0.997	0.994	0.995	0.996	0.999	0.999
LOD (nmol/l)	15.56	6.85	8.99	4.42	5.98	5.88	4.82	2.06	2.58
S ($nA.nmol^{-1}l.mm^{-2}$)	10.729	22.073	22.017	21.910	40.21	36.842	19.861	26.14	20.835
RSD (n =100) (%)	8.43	3.56	21.85	7.61	4.68	26.78	11.95	4.83	26.75
GDOES (%)	2.019			1.8424			1.862		

Based on the above-presented results, BDD electrodes seem to be an attractive alternative to MFE. Several functional BDD electrodes have been used for determining Zn, Cd, Pb with in-situ Bi plated electrodes. Measurements with different B/C ratio of BDD were compared and BDDE with 10 000 ppm it shown as a best electrode for next microelectronic research. Excellent properties of highly doped BDD based on in-

situ Bi electroplating exhibited good performances in terms of high sensitivity, low limit of detection and relative standard deviation (RSD).

Acknowledgements

Authors would like to thank to J. Král for technical support. This work was done with a support of Slovak Research and Development Agency project No. LPP-0094-09, APVV-0548-07, VEGA projects 1/1103/11 and 1/1102/11 and DAAD project 507 552 00.

References

[1] Paul W. May: Diamond thin films: a 21st-century material in Phil. Trans. R. Soc. Lond. A (2000) 358, 473–495
[2] V. Rehacek et al., Nafion-coated bismuth film electrodes on pyrolyzed photoresist/alumina supports for analysis of trace heavy metals in Electrochimica Acta 63 (2012)192-196
[3] E. A. McGaw, G.M. Swain: A comparison of boron-doped diamond thin-film and Hg coated glassy carbon electrodes for anodic stripping voltammetric determination of heavy metal ions in aqueous media In Electrochimica acta 2 (2006) 180-189
[4] R.Trouillon, D O´Hare: Comparison of glassy carbon and boron doped diamond electrodes: Resistance to biofouling in Electrochimica Acta 55 (2012) 6586-6595
[5] Thanh Son Le et. al., Upstream microelectrodialysis for heavy metals detection on boron doped diamond in Journal of Electrochemical Chemistry 670 (2012) 50-55
[6] T. Watanabe et. al., Giant electric double-layer capacitance of heavily boron-doped diamond electrode in Diamond & Related Materials 19 (2010) 772–777
[7] S.-Tong Lee, Zhangda Lin, Xin Jiang: CVD diamond films: nucleation and growth in Materials Science and Engineering, 25 (1999) 123-154
[8] M. Bernard et al., Non-destructive determination of the boron concentration of heavily doped metallic diamond thin films from Raman spectroscopy in Diamond and Related Materials 13(2004), 282-286

Enhancement of fingerprint topology by sputtered nano-columnar thin films

V. Tvarozek [1)], S. Flickyngerova [1)], I. Novotny [1)], V. Rehacek [1)], D. Rossberg [2)], T. Kups [2)], P. Schaaf [2)] and P. Sutta [3)]

[1)] Slovak University of Technology, Institute of Electronics and Photonics FEI, Ilkovicova 3, 81219 Bratislava, Slovak Republic
[2)] Ilmenau University of Technology, Institute of Materials Engineering and Institute of Micro- and Nanotechnologies, POB 100565, 98684 Ilmenau, Germany
[3)] University of West Bohemia, New Technologies Research Centre, Univerzitni 8, 30614, Plzen, Czech Republic

Abstract

The homogenous coating of fingerprints by transparent/conductive Al doped zinc oxide (ZnO:Al) thin films via RF diode sputtering is presented. The possibility to deposit nano-columnar ZnO:Al films by sequential RF diode sputtering and their applicability in an enhancement of fingerprint topology are proven.

1 INTRODUCTION

Fingerprints are unique to an individual person and they are important for the identification and evidence of citizens as well as for the criminology. Modern fingerprints-development techniques are mostly based on the chemical composition of the fingerprint residue or emulsion but none of them exclusively explore the topology of the fingerprint residue. Shaler et al. [1] proposed to use columnar thin films prepared by physical vapour deposition for visualization of fingerprint topology. They developed the conformal-evaporated-film-by-rotation technology to deposit dense columnar thin films (chalcogenide glass, MgF_2 or Au) on latent fingerprint [2]. The principle corresponds to the 3D Pin Art Sculpture or a Pin Point Impression child's toy, Fig. 1a [3].

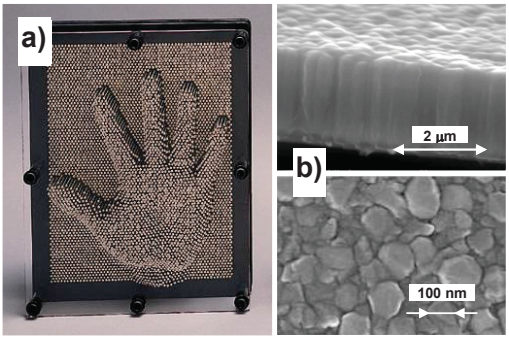

Fig. 1: a) PinPressions Metal 3D Pin Art Sculpture Toy and b) SEM images of the columnar grain structure and surface morphology of sputtered ZnO thin films.

Optically transparent and electrically conductive oxide (TCO) thin films based on ZnO have many applications in transparent electronics and thin film solar cells [4]. RF diode sputtering (at usual technological conditions)

leads to strongly textured polycrystalline TCO thin films with columnar grain structure preferentially oriented along c-axis normally to the substrate, Fig. 1b [5]. Columnar crystalline (002) structure was also dominant for sputtering of Al-doped ZnO (ZnO:Al) thin films. Previous results confirmed that RF diode sputtering has a beneficial feature to coatings of three-dimensional samples in comparison with magnetron sputtering [6].

Our aim was to prove the possibility to deposit nano-columnar ZnO:Al films by RF diode sputtering and their applicability in an enhancement of fingerprint topology.

2 Experimental Details

We used two modes (continual and sequential) of RF diode sputtering, Perkin Elmer system 2400/8L, ZnO+2% Al_2O_3 target of 153.2 mm in diameter, Ar pressure of 1.3 Pa, sputtering power of 600 W, Fig. 2. ZnO:Al films (thickness of 100 nm) were continually deposited on both Corning glass and Silicon planar substrates with fingerprints at the nominal rate of 0.20 nm/s. A sequential sputtering layer-by-layer (1 nm–by–1 nm) of ZnO:Al thin films with total thickness of 100 nm was used for the covering of fingerprints at the nominal rate of 0.13 nm/s.

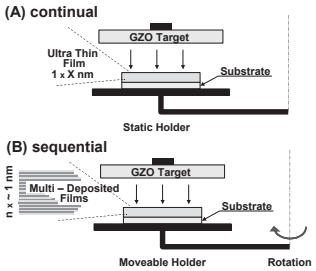

Fig. 2: Schematic layout of continual and sequential sputtering.

X-ray difraction patterns of ZnO:Al thin films were recorded on a thin film attachment of an X`pert Pro powder diffractometer (Cu Kα, λ = 0.154 nm). Microstrain-crystallite size evaluations were performed using a method proposed by Langford based on the XRD line profile analysis [5]. Visualization of fingerprints was done by optical microscopy, surface and cross-section by Scaning Electron Microscopy SEM / Focused Ion Beam FIB SEM Auriga 60 ZEISS.

3 Results

Nanocrystalline structure of sputtered ZnO:Al films depended on the mode of sputtering: films deposited continually showed polycrystalline structure preferentially oriented in c-axis direction, (Fig. 3), whereas sequential sputtering produced stronger (002) texture. From the diffraction line position shift and the Cauchy component of the integral breads of the line according to the Bragg law and the Scherrer´s formula [5] were quantitatively evaluated biaxial lattice strains (stresses) and

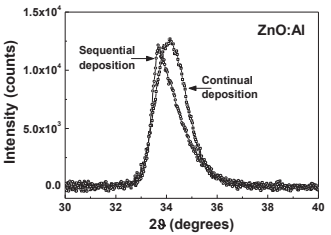

Fig. 3: XRD lines of nano-columnar ZnO:Al films (thickness of 100 nm) deposited by continual and sequential sputtering.

crystallite sizes. Sequential sputtering causes higher compressive lattice strains in films ($< \varepsilon > \approx 10^{-3}$) when compared with the continual mode ($< \varepsilon > \approx 10^{-2}$). The average size of crystallites evaluated from XRD measurements was in agreement with the size of nanocrystals observed in TEM (an order of 10 nm). Continually sputtered films showed average size of nanocrystals ($< D > \approx 40$ nm) in comparison with sequentially deposited films ($< D > \approx 50$ nm). Both modes of sputtering created nanocolumnar thin films, Fig. 4. The sequential deposition formed less dense multilayered ZnO:Al film which is in agreement with previous observations concerning ZnO:Ga coatings [6].

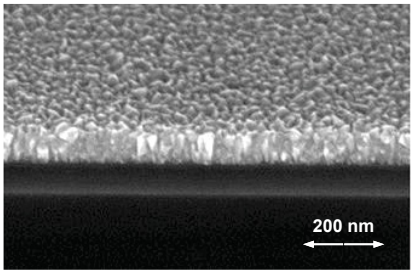

Fig. 4 Surface and cross-section SEM images of nano-columnar ZnO:Al films (thickness of ≈ 100 nm) deposited on clean Si substrate by continual sputtering.

Optical images of sebaceous fingerprints on Si or Corning glass are shown in Fig. 5a and Fig. 6.

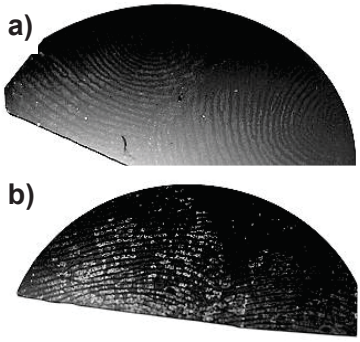

Fig.5: Optical images of fingerprint on Si: (a) a sebaceous fingerprint; (b) covered by ZnO:Al film of 100 nm in thickness via continual sputtering.

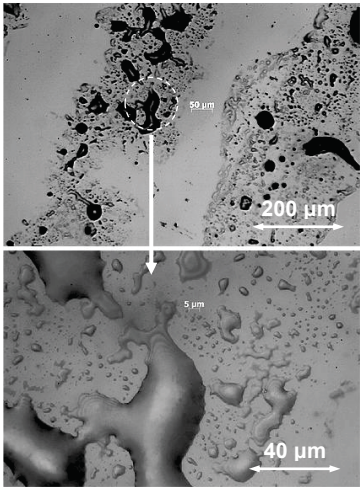

Fig. 6: Optical images of sebaceous fingerprint topology details on Corning glass.

Sputtering of ZnO:Al thin films (100 nm in thickness) on the fingerprint emphasized its topographical features observed particularly by optical microscopy (Figs. 5b, 7, 8). Sharp ridges were formed on thicker fingerprint constituents and mosaic texture of surface appeared on places with very thin fingerprint residues, Fig. 7 and 8. Self-heating of substrates during the continual sputtering caused a noticeable degradation

of the initial fingerprint morphology, particularly by using Si substrate (Figs. 7a and 8a). The sequential sputtering did not change the initial fingerprint morphology and improved image resolution obtained by both the optical microscopy (Figs. 7b and 8b) and the scanning electron microscopy (Fig. 9). ZnO:Al films grown on fingerprint remained their nano-columnar crystalline structure (Fig. 10).

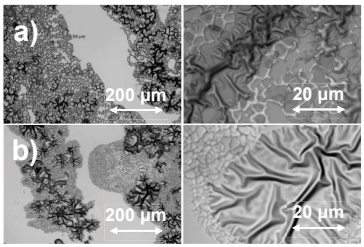

Fig. 7: Optical images of fingerprint ridge details on Corning glas covered by continual (a) and sequential (b) sputtering of ZnO:Al film (100 nm).

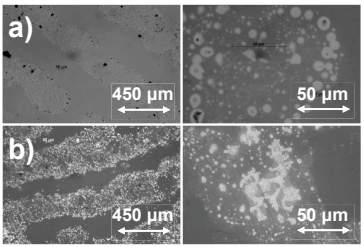

Fig. 8: Optical images of fingerprint ridge details on Si substrate covered by ZnO:Al films (100 nm) via continual (a) and sequential (b) sputtering.

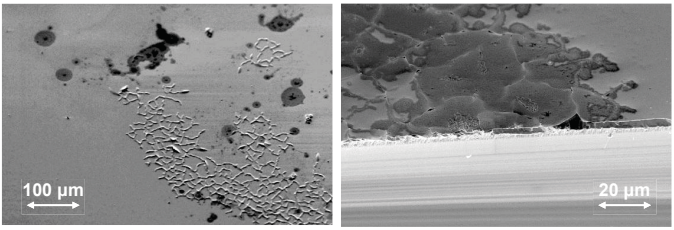

Fig. 9: SEM images of fingerprint surface details (covered by ZnO:Al film).

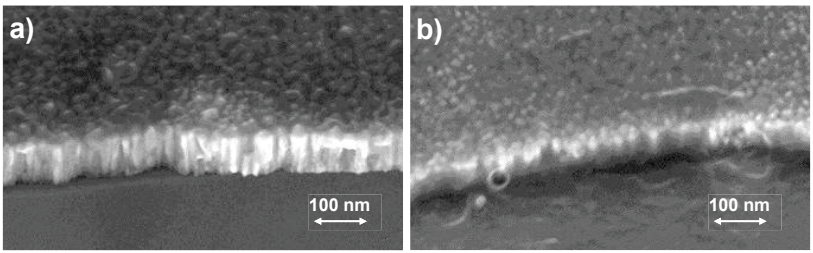

Fig. 10: Surface and cross-section SEM images of nano-columnar ZnO:Al films (thickness of ≈ 100 nm) deposited on fingerprint by continual (a) and sequential (b) sputtering.

4 DISCUSSION

On the base of these results and our experience with continual sputtering we decided primarily to exploit sequential sputtering for covering of fingerprints. Experiments obtained using ZnO:Al material to visualize latent fingerprints demonstrated that nanocolumnar thin films were grown by sputtering on fingerprint residues. High optical transparency of ZnO:Al films together with their columnar structure highlighted fingerprints details observed by optical microscopy. Observations of fingerprint topology by SEM are limited by scale because there are different amount of sebaceous secretions present in various areas of the print which are corresponding to objects of mm/μm – dimensions.

One of the noticeable outputs of presented results is given by the forming of nanocolumnar crystalline thin films with nanoscale thicknesses by sputtering. It opens the way for application of these transparent and (semi)conductive films in optoelectronics as well as in the light management in thin film solar cells.

5 CONCLUSIONS

RF diode sputtering led to the formation of the homogenous nano-columnar thin films on the fingerprint thereby enhancing its topographical texture with higher resolution in comparison with a sebaceous one. Advantages of this technology are: sputtered ZnO:Al thin films are transparent and conductive, they are likely to create columnar structure, they do not react with the fingerprint residue and the sequential sputtering improves crystalline structure and minimizes the self-heating of the substrate. Presented method is one example of so-called impression evidence and it needs further development and comparison with the other methods for the capturing of fingerprint topology, e.g. use of evidence tape.

Acknowledgements

Presented work was supported by the DAAD Project 50755200 NanoMat, the SK VEGA Project 1/0459/12 and partially by the CZ CENTEM project no. CZ.1.05/2.1.00/03.0088 co-funded from the ERDF OP RDI programme of the MEYS CR.

References

[1] R.C. Shaler, A. Lakhtakia, J.W. Rogers, D.P. Pulsifer, R.J. Martin-Palma: Columnar-thin-film acquisition of fingerprint topology, J. of Nanophotonics, Vol. 5, 051509/1 – 10, 2011.

[2] A. Lakhtakia, R.C. Shaler, R.J. Martin-Palma, M.A. Motyka, D.P. Pulsifer: Solid-State Acquisition of Fingermark Topology using Dense Columnar Thin Films, J. of Forensic Sciences, Vol. 56, No. 3, 612 – 616, 2011.

[3] http://www.alibaba.com/products/gs-328972529/3D_Pin_Art_Gift.html.

[4] Ü. Özgür, Ya.I. Alivov, C. Liu, A. Teke, M.A. Reshchikov, S. Doğan, V. Avrutin, S.J. Cho, H. Morkoç: A comprehensive review of ZnO materials and devices, J. of Applied Physics 98, 041301/1 – 103, 2005.

[5] V. Tvarozek, P. Sutta, S. Flickyngerova, I. Novotny, P. Gaspierik, M. Netrvalova, E. Vavrinsky: Preparation of transparent conductive AZO thin films for solar cells, Chapter 12, pp. 271 - 294, In: Semiconductor Technologies, Jan Grym (Editor), Publisher: In-Tech, pp. 462, ISBN 978-953-307-080-3, 2010.

[6] I. Novotny, V. Tvarozek, P. Sutta, M. Netrvalova, J. Novak, I. Vavra, P. Elias: Preparation of shell nanocrystalline Ga-doped ZnO ultra-thin films by sputtering, Proceedings of 28th Int. Conf. on Microelectronics MIEL 2012, ISBN 978-1-4673-0235-7, 269 - 271, Nis, Serbia, 2012.

Detection and correction of measurement data errors in magnetic and electromagnetic non-destructive testing of materials

D.A. Slesarev

MPEI (TU), Moscow

1 INTRODUCTION

Structural integrity and reliability of construction elements in power engineering systems depend to a considerable extend from state and characteristics of there material. This can be obtained by means of different methods of non-destructive testing, which for metallic materials in most cases means – electromagnetic or acoustic methods. In this cases material is exposed to external electromagnetic or acoustic excitation and the distribution of resulting reaction over the surface is to be measured. In the case of electromagnetic testing this means distribution of electromagnetic field. Estimation of material characteristics is to be made by means of inverse problem solution. In many cases, material discontinuities should be detected and their size be estimated, for example pipe wall continuousness faults. Modern instruments, which enable solution of this problem, consist mostly of sensor lattices and arrays and data processing units. Application of sensor arrays (lattices) enables high degree of data processing automation and raises test feasibility. With increasing of element number in sensor arrays increases also a probability of sensor faults and consequently errors and failure in measurement data. Such failures can be especially critical for solution of inverse problem because of its instability. In this connection detection and correction of sensor malfunction has great importance in measurement systems with sensor arrays (in particular high resolution sensor arrays).

2 PROBLEM ANALYSIS

Detection sensor malfunction and correction of measurement errors will be shown on an example of magnetic non-destructive testing of steel plates or pipes. To detect sensor malfunction different criteria are applied, which assume correct calibration of measurement system relative recorded values. In this case permissible variations of measured value should not exceed dynamic range of measurement system at a given system sensitivity. So a prolonged saturation of sensor signal can be used as a first criterion of sensor malfunction. The second sensor malfunction criteria is based on the assumption, that random influence factors effects all sensors to the same extend, consequently a standard deviation of sensor measured value should not differ significantly from an average standard deviation of the sensor array:

$$\sigma_i^2 < \sigma_{mean}^2 / k_2$$

where σ_i^2 - variance of the *i*-th sensor, σ_{cp}^2 - average variance of the sensor array, k_2 – some coefficient (k_2>1). Coefficient k_2 is to be chosen with a consideration of characteristics of measurement system and measured. Often more complicated criteria are applied to detect sensor malfunction. To detect missed scans scan numeration is applied.

Correction of detected measurement errors, caused by sensor malfunction is based on the model of expected signals. This model can be built with helps of a priori information about inspected objects, which often enables parameterization of the model. As an example Figure 1 shows typical signal, obtained by the measurement of magnetic field distribution above a pitting corrosion on the pipe wall in the applied magnetic field (B_z - axial component of magnetic field). Such signals appear in magnetic non-destructive testing [1]. Parameter of this signal carries information about defects size.

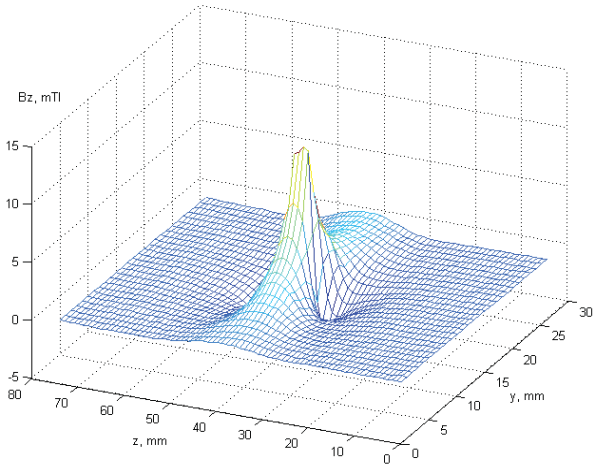

Figure 1. Typical signal of magnetic field distribution above a pitting corrosion on the pipe wall

Malfunction of sensors leads to a mistake in the estimation of material discontinuities. For example estimation of the corrosion depth made by regression method [1] for a pitting corrosion with diameter of 24 mm gives as a result 1.8 mm (real depth 1.6 mm) with no sensor malfunction and 2.6 mm with a malfunction of one sensor block in sensor array. The measurement signal for this situation is shown on Figure 2. Estimation error for the signal with malfunction sensors makes up 0.13T instead of 0.03 T (where T – wall thickness, is 8 mm), which is 4 time more, than in normal case.

Error correction is based on the redundancy of measurement data, which means in the case of non-destructive testing a certain margin of sensitivity and resolution relative minimal detectable defect.

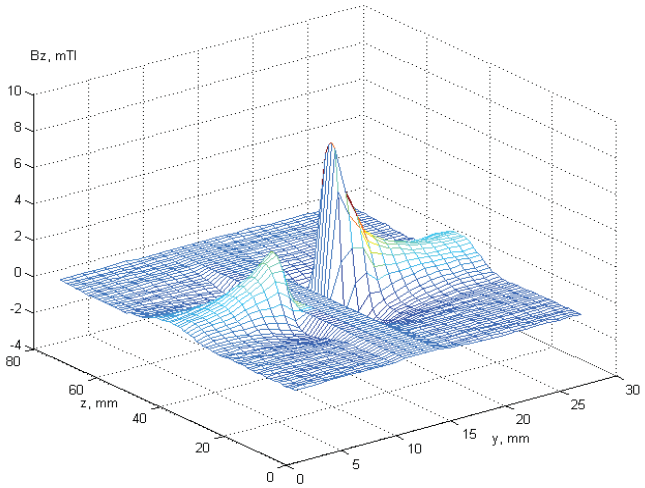

Figure 2. Signal of magnetic field distribution of pitting corrosion with a malfunction of one sensor block.

When detecting sensor malfunction, its reading should be substituted by a value, calculated on the base of neighbouring sensors reading. In most of cases these values are calculated by means of interpolation. Different types of interpolation can be applied, but the mostly widespread are piecewise constant, piecewise linear and spline interpolation. These three types are compared below on the example of the signal, shown on the Figure 2.

3 RESULTS

Figure 3 depicts application of piecewise constant (a), piecewise linear (b) and spline (c) interpolation to a central profile of the signal in the Figure 2.

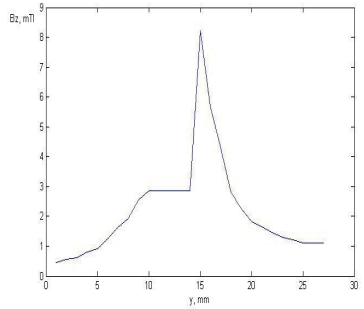

a

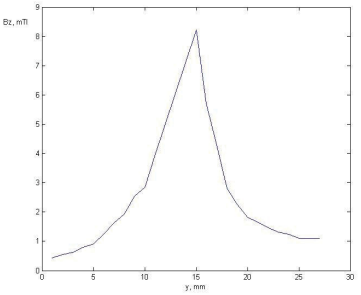

b

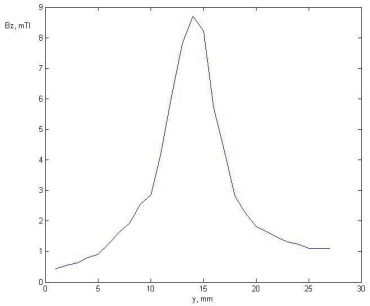

c

Figure 3
Piecewise constant, piecewise linear and spline interpolation of malfunction sensor block.

Piecewise linear interpolation consists in substitution of faulty sensors reading with ones, calculates as linear approximation of corresponding samples on the base of the neighbouring good sensors. Correct realization of this type of interpolation assumes additionally analysis of faulty sensors location – at signal extremum or in monotonous region. In the first case interpolation region should be divided into two parts – each should be calculated separately. This type of interpolation presumes 2 multiplications for each erroneous sample.

Spline interpolation consists in the calculation of faulty sensors reading on the base of the neighbouring good sensors with helps of spline functions – mostly cubic splines. Number of supporting sensors depend on the degree of spline, it is necessary at least 2 supporting sensors from each side of faulty sensors. This type of interpolation is most resource-demanding and complicated in realization. An appropriate algorithm demands 12 multiplications for each erroneous sample in within several consequent cycles.

This three interpolation methods were compared at the sampling of material discontinuities of different size [2]. The sampling consisted of artificial defects of round and square shape with characteristic size from 12 mm to 36 mm and depth of

1.5 mm to 6 mm (wall thickness – 8 mm). Sensor malfunction was simulated in two different regions of signal – at signal extremum and in monotonous region. Average error of defects depth estimation for different types of interpolation is given in the table 1. One can see that for sensor malfunction at the edge even piecewise constant interpolation allows reducing estimation error to 0.03 T. For sensor malfunction in the centre of the signal defect depth estimation with piecewise constant interpolation has rather big error – 0.14 T. With help of spline interpolation this error can be reduced to 0.08 T.

Table 1. Average error of defects depth estimation for different types of interpolation

	Interpolation type		
	piecewise constant	piecewise linear	spline
Sensor malfunction at the edge	0,2 мм	0,16 мм	0,15 мм
Sensor malfunction in the center	1,1 мм	1,0 мм	0,69 мм

4 CONCLUSIONS

Thus best results of measurement errors correction can be achieved with help of spline interpolation and it enables to reduce the error of material discontinuities depth estimation for the case of central sensors malfunction to 0.08 T. This method is nevertheless significantly more resource-demanding than piecewise constant or piecewise linear interpolation. In many cases it is sufficient to apply piecewise linear interpolation.

Acknowledgements

I express my thanks to “INTRON PLUS” Company (Moscow) for support of this reseach.

Literature

[1] Slesarev D.A., Barat V.A. Statistical diagnostic model for Defect parameters reconstruction in MFL nondestructive testing. 10-th European Conference on Non-Destructive Testing - Moscow, 2010, p. 50.

[2] Slesarev D.A. DETECTION AND CORRECTION OF MEASUREMENT DATA FAILURE IN MFL NON-DESTRUCTIVE TESTING, Kontrol. Diagnostika, 2012, №5.

A Study of Temperature Dependence of Self Absorption Limit of the Single Crystals In_2S_3

Polubok Uladzislau A.

Belarusian State University of Informatics and Radioelectronics.
Institute of Information Technology

Abstract

The Bridgman and Bridgman–Stockbarger techniques have been implemented to synthesize and grow the single crystals of binary compound In_2S_3, which have been used as a basis to getting further some samples of high temperature cubic modification. The transmittance spectra of these samples have been removed. The obtained data helped to define the self-absorption limits and to find the dependence of the self-absorption limits on the temperatures.

1 INTRODUCTION

Diamond-like semiconductors are widely known because of the combination of some important semiconductors' properties: high carrier mobility, photo- and thermoelectric qualities, low thermal conductivity. At the same time, while studying properties of the nonorganic semiconductor compounds with a normal structure, like sphalerite or wurzite, the compounds with a defect structure have been either studied. When compared to the analogue compounds of Type $A^{III}B^{V}$ or $A^{II}B^{VI}$, the compounds of type $B_2^{III}C_3^{VI}$ (where B^{III} – B, Al, Ga, In, Tl; C^{VI} – S, Se, Te) demonstrate some special properties due to their defect structure.

The single crystals In_2S_3 arouse interest because of their properties as follow: high radiation resistance, conditioned by a big number of defects (~33 %); forbidden zone width which is close to the optimal one (Eg = 1,9 – 2,2 eV) for design of the solar radiation converters; possibility to replace the toxic CdS in production of the solar radiation converters. Combined, all these properties may make this compound useful for different technical devices: LED of linearly polarized radiation, solar radiation photoconverters of high efficiency (~ 12 – 18%) [1,2].

2 EXPERIMENTAL DETAILS

Previous synthesis of the binary compound In_2S_3 has been realized by directional crystallization technique (horizontal version of the Bridgman technique), when the metallic Indium and Sulfur are placed in different parts of a quartz vessel. First the temperature in the "hot" part of the oven had been raised at the speed of~ 50 K/h up to 1380 – 1400 K, and in the "cold" part – up to ~ 770 K. At these temperatures the isometric soak was 1 hour long. After that, the directional crystallization was carried out by means of the melt temperature decrease at the speed of ~5 K/h down to

670 K, while the temperature of the "cold" one was constant ~ 770 K, the obtained crystals were annealed for 150 hours. Then, the oven should have been disconnected. The crystals we obtained that way were large-grained, some of the grains were (20 – 25)x10x5 mm^3.

The derived crystals were used to grow single crystals according to the Bridgman-Stockbarger technique. Evacuated to 10^{-3} Pa and sealed ampoule was placed into the upper zone of three-zone vertical oven. The temperature of the melting zone was established at ~ 1400 K. The ampoule in the oven with melting remained for ~ 24 hours in order to homogenize the melt and then was moved down through the crystallization front into the lower zone at the speed of ~ 0,18 mm/h at temperature gradient ~ 40 K/cm.

In the initial stage of the growth process the conditions of the preparation of the single crystal seed were chosen. In order to get the crystal seed, a part of melt (~ 7 mm long) was crystallized by sinking the ampoule, after that the crystallizing annealing was held for 72 hours. That way we formed a single inoculating crystal as a basis for further In_2S_3 crystals growing. When the melt is crystallized, the crystals we got should be annealed for 150 h at the temperature of 1020 K. In these conditions the single crystals In_2S_3 20 mm diameter and 50 mm (fig. 1) were grown.

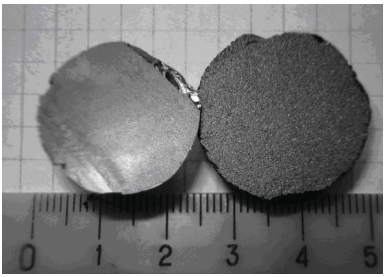

Figure 1 – Single crystal of the binary compound In_2S_3

The same technique was used to obtain a high temperature modification. What makes different the technological process is that when the temperature exceeded the phase transition temperature (~ 700 K), the wire which was used to sink the ampoule into the oven, was cut the way the ampoule felt down to the vessel filled with liquid nitrogen. Then the samples were quenched.

The element content of the grown crystals [In]:[S]=39,75:60,25 at % coincide with the required composition of the initial load [In]:[S]=40,00:60,00 at %, and there are no significant variations of the composition while analyzing in different points, which means it is uniform. According to the obtained data, the grown crystals composition coincide with the formula of In_2S_3.

The X-Ray studies were made on the samples previously prepared by pulverizing the crystals. In order to improve mechanical stresses while pulverizing crystals, they were annealed in vacuum at 973 K for 72 h.

For optical measurements some plane parallel segments were cut out the crystal perpendicular to its growing axis. Then, these derived wafers were grinded and polished. As a result of grinding and polishing we got few samples 20 micrometers wide.

To define energies of the optical transition in the crystals and their dependence on the temperature, the spectra of optical transmission for waves 0,5 – 0,8 micrometers long and temperature range 20 – 300 K were measured.

3 RESULTS

The derived X-Ray patterns were indexed, the double grazing angle values for all the diffraction maxima were determined with accuracy up to centigrades.

On the diffraction patterns (fig. 2 and fig. 3) we see a system of lines which correspond to the tetragonal structure (fig. 2) and cubic (fig. 3). The elementary cells data were calculated using least-square method for reflexes at angles 2θ > 60º. The elementary cell data is a = 7,618 ± 0,005 Å, c = 32,25 ± 0,05 Å for tetragonal modification and a = 10,77 ± 0,01 Å for cubic modification, thus correspond to the facts [2.3].

The transmission coefficients of the single crystals of two modifications were evaluat-

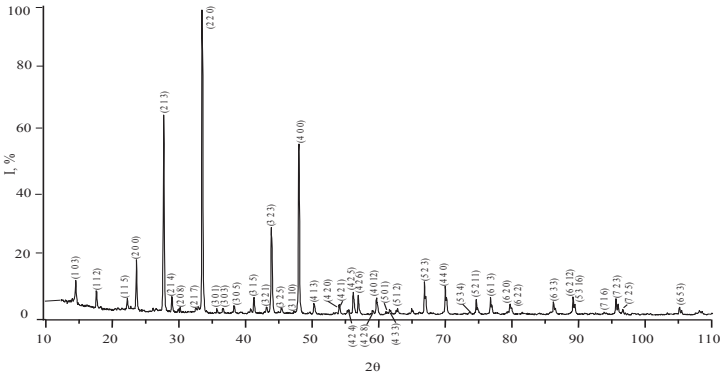

Figure 2 – Diffraction pattern of the In_2S_3 crystal of tetragonal modification

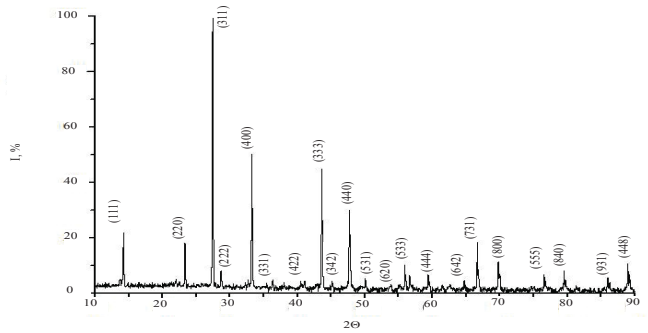

Figure 3 – Diffraction pattern of the In_2S_3 crystal of cubic modification

ed experimentally. The results can be seen in fig. 4.

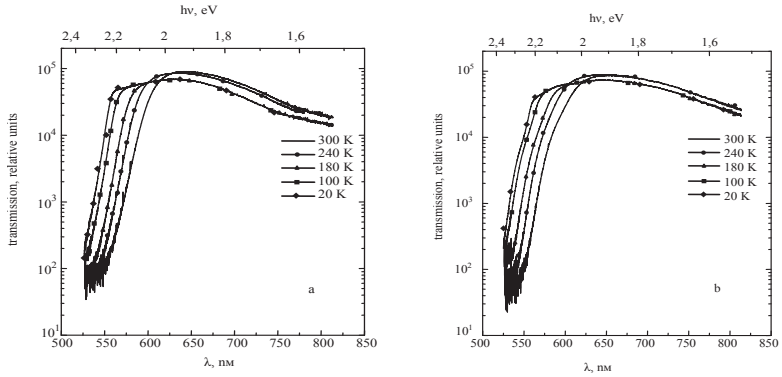

Figure 4 – Dependence of transmission on the wave length for cubic (a) and tetragonal (b) modifications at different temperature degree.

4 DISCUSSION

The absorption coefficient α was calculated basing on the registered transmission spectra according to the formula that considers multiple internal reflections in plane parallel sample:

$$\alpha = \frac{1}{d}\ln\left(\frac{(1-R)^2}{2T} + \sqrt{\frac{(1-R)^4}{4T^2} + R^2}\right)$$

where d — sample thickness;

R — reflection coefficient (R=0,25);

T — transmission coefficient.

The spectral dependence $(\eta\ h\nu)^2$ on the photon energy (hv) for cubic and tetragonal modifications was determined (fig.5).

The values of self-absorption limit (Eg) were found by extrapolation of straight-line segment of the dependence $(\eta \cdot h\nu)^2$. Eg values at different temperature grades may be seen in the table 1.

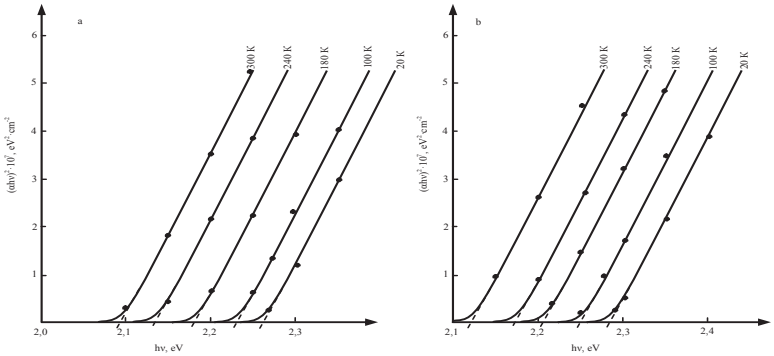

Figure 5 – Spectral dependence $(\alpha \cdot h\nu)^2$ on the photon energy ($h\nu$) at the temperature range (20 — 300 K) for single crystals In_2S_3 of cubic a) and tetragonal b) modifications

Table 1 – Values of the forbidden zone width for In_2S_3 of two structural modifications at different temperatures

Cubic modification		Tetragonal modification	
T, K	Eg (T), eV	T, K	Eg (T),eV
20	2,27	20	2,29
100	2,23	100	2,24
180	2,18	180	2,21
240	2,13	240	2,18
300	2,09	300	2,13

In fig. 6 you may see the temperature dependence of the self-absorption limit.

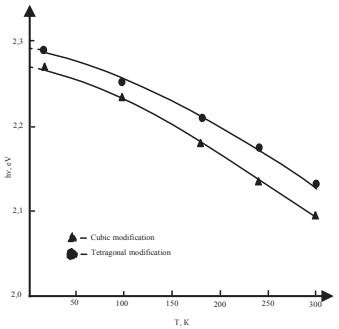

Figure 6 – Dependence of the self-absorption limit energy for direct transition on temperature for single crystals In_2S_3 of two structural modifications

5 CONCLUSIONS

The single crystals of tetragonal modification were grown using Bridgman and Bridgman-Stockbarger techniques. The technique for the preparation of the single crystals of In_2S_3 with cubic modification is presented. By X-Ray spectral analysis technique we proved that the composition of the grown crystals coincide with the In_2S_3 formula. The grown single crystals of two structural modifications were studied in order to see the dependence of the self-absorption limit on the temperature. The results we see on the fig. 5 show that the dependence has some clear straight-line segment which means (as well as the X-Ray data) equal-weighting and uniformity of the grown single crystals. It was also proven that when the temperature increases, the self-absorption limit decreases.

Acknowledgements

I would like to thank my teacher Professor Bodnar I.V.

References

[1] Sebentritt S. Alternative buffers for chalcopyrite solar cells. // Solar Energy. – 2004. – Vol.77. – P. 767 – 775.
[2] Influence of In_2S_3 film properties on the behavior of $CuInS_2/In_2S_3/ZnO$ type solar cells. Asenjo B., Chaparro A.M., Gutierrez M.T., Herrero J. et all. // Solar Energy Materials & Solar Cells. – 2005. – Vol. 480 – 481. – P. 151 – 156.
[3] Rooymans C.I.M. A new type of cation – vacancy ordering in the spinel lattice of In_2S_3. // J. of Inorg. And nucl. Chem. – 1959. – Vol.11. – №11. – P 78 –79.
[4] Steigman G.A., Sutherland H.H, Goodyear J. The crystal structure of β-In_2S_3 // Acta Cryst. – 1965. – Vol.19. – №6. – P. 967 –971.

Incorporation of Copper Nanoparticles into DLC Films during Growth by DC PE-CVD Method

Marian Marton[1], Mário Kotlár[1], Pavol Michniak[1], Marcus Wilke[2], Rolf Grieseler[2], Marcus Hopfeld[2], Peter Schaaf[2], Marian Veselý[1]

[1]Institute of electronics and photonics, FEI STU, Ilkovičova 3, 84104 Bratislava, Slovakia
[2]Institute of Materials Engineering, Chair Materials for Electronics, Ilmenau University of Technology, Ilmenau 98694, Germany

Abstract

Metal doped diamond-like carbon (Me-DLC) thin films were deposited using DC PECVD deposition process in CH_4/Ar plasma. Cu was incorporated into the films by sputtering a negatively biased target with Ar ions while DLC was produced from CH_4 as carbon source. The influence of deposition parameters on the size and density of metal nanoparticles was studied. Methane and argon flow ratio, gas pressure and substrate bias were changed to obtain high metal concentration. The presence of metal particles led to increased electrical conductivity of the highly resistive DLC layers and changed it in several orders of magnitude. The effect of annealing and plasma etching were also observed. The surface morphology and structural properties of the synthesized thin films were evaluated by SEM (LABE), GDOES and Raman spectroscopy.

1. INTRODUCTION

Diamond-like carbon, i.e. the amorphous network of sp^2 and sp^3 bonded carbon atoms has attracted attention for its extraordinary properties, such as high hardness and wear resistance, low friction coefficient, biocompatibility, transparency in IR, wide potential window and chemical stability. These properties make them suitable for various applications in the field of cutting tools, automotive industry, artificial human body parts, optics, electronics and sensors [1]. The main disadvantage for the use of DLC in the field of electronics is the low conductivity caused by high concentrations of sp^3 C-C and C-H bonds in the films. Therefore, there are many attempts to increase the conductivity by film doping. The most used doping elements to be incorporated into the amorphous carbon network are nitrogen, boron and various metals [2-6].

The electrical conductivity of amorphous carbon films may be tuned by up to 12 orders of magnitude – from an insulator to a metallic conductor – by adding Au and Ta metal atoms into the growing films. The metal atoms are not homogeneously distributed in the carbon or hydrogenated carbon material; instead metal clusters or metal carbide clusters are formed due to the aggregation processes during the film formation.

This heterogeneous material consists of crystalline conducting metal clusters embedded in a more or less insulating matrix of amorphous carbon which may be hy-

drogenated as well (Me:a-C:H). Tunneling or hopping of the carriers between the metallic islands was suggested as the dominant conduction mechanism [7]. In this work, the preparation of copper doped DLC (Cu-DLC) films by the DC PE-CVD method is studied.

2. EXPERIMENTAL

DLC thin films were deposited by a DC PE-CVD process in a vacuum reactor (UVNIPA-1-001) described previously in Ref. [8] using a DC power supply. Mirror polished Si and Corning glass substrates were used for deposition of the coatings. Prior to deposition, substrates were cleaned for 20 min with Ar ions within the deposition chamber. Background pressure was 10^{-1} Pa and working pressure was maintained from 3 to 8 Pa depending to the gas flow. Methane was used as precursor gas for DLC growth, while the admixture of argon was responsible for simultaneous sputtering of copper target. The deposition voltage was changed from -1 to -4 kV and the temperature was below 200 ºC. The Cu-DLC composite layers were subsequently annealed at 300 °C and 500 °C under 10^{-2} Pa vacuum using rapid thermal annealing (RTA) for one hour. The resistivity of the films was measured before and after the annealing process employing the van der Pauw method. The structural properties of DLC films were evaluated by scanning electron microscopy (SEM, JEOL 7500F) using secondary electron imaging (SEI) and Raman spectroscopy with 632.8 nm radiation from a He–Ne laser. The acquired Raman spectra were fitted with a Gaussian line to illustrate the D and G peak positions and the G peak full width at half maximum (FWHM).

3. RESULTS AND DISCUSSION

Raman spectra of the as deposited and annealed DLC films presented in Fig.1 show the typical D and G band at 1,350 and 1,580 cm^{-1} associated with disordered (D) and graphite (G) sp^2 C-C bonds. The data from fitted Raman spectra of the annealed films are depicted in Fig.2.

With increased annealing temperature, the G peak position increased towards the value of graphite and the FWHM decreased, which means the film became more crystalline. From SEM images shown in Fig. 3 and the Raman spectra we can assume that, with increasing of the annealing temperature, the films became more graphitic.

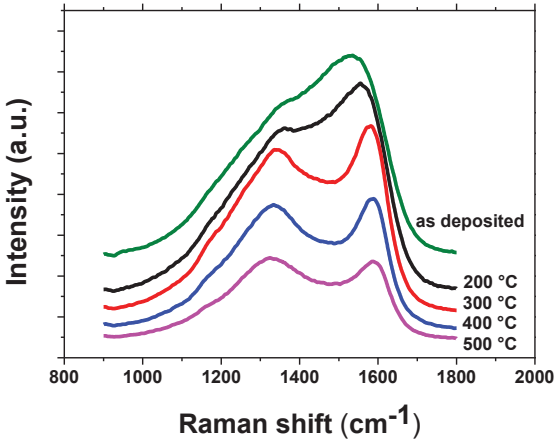

Fig.1: Raman spectra of as deposited and annealed DLC layers. Annealing temperature is given in the figure.

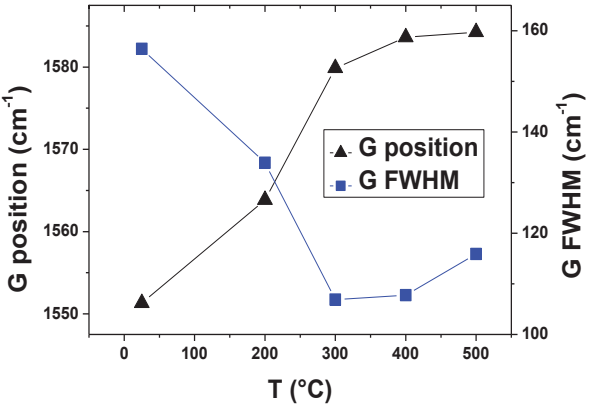

Fig.2: Dependence of G peak position and its FWHM on annealing temperature

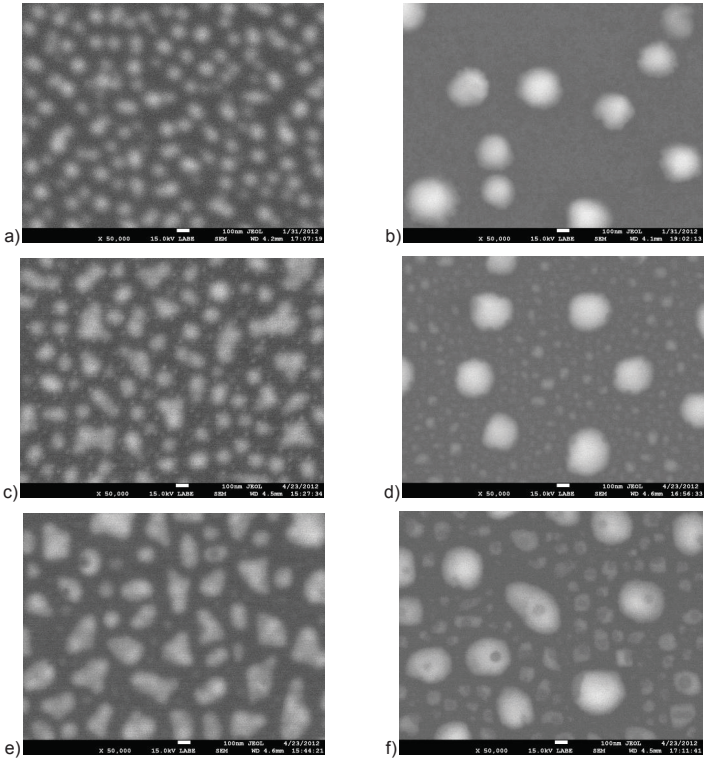

Fig.3: *SEM images of as deposited (a,b) and annealed (c,d – 300°C, e,f – 500°C) Cu-doped DLC films, marker shows 100 nm.*

Fig. 3 presents SEM images of the films. Fig. 3 a), b) shows two different deposited Cu-DLC films. The bright dots are the copper particles deposited homogenously within the films. We can see that the size of the copper particles and distances between them changed with the different deposition conditions. The average size of copper particles varied from tenths to hundreds of nm. The images c) and d) show the layers annealed at 300 °C and e) and f) are the layers annealed at 500 °C. In the case of first layer, after annealing at 300 °C we can observe small Cu particles appeared in the empty space in between the previously deposited larger particles. After annealing at higher temperature, there are still new small Cu particles and all of the particles seem to join together creating larger clusters. After annealing of the next layer (Fig.3 d) at 300 °C, there are the new small particles between the deposited ones again. It is clear from the image taken from layer annealed at 500 °C that the origin of them is in the larger as deposited particles which contain holes and empty spaces. After annealing process, the distribution of Cu over the DLC thin films seems to be much

more homogenous and distances between conductive Cu particles are visibly smaller.

While the bulk resistance R_{bulk} of the non-doped DLC thin films was not measurable (i.e. it was extremely high), the values of the resistivity of the as deposited Cu-DLC layers were measured to be in the range from 10 Ω·cm to 6×10^{3} Ω·cm, depending on deposition properties and thus the resulting amount, size and distribution of Cu particles in the films. After annealing the process at 500 °C, the resistivity drops by several orders of magnitude to values ranging from 4×10^{-2} Ω·cm to 3 Ω·cm.

4. CONCLUSIONS

We used PECVD method for the deposition of Cu incorporated DLC thin films from CH_4/Ar gas mixture. The size of the nanoparticles varied with changing the deposition conditions in the range of tenth to hundreds of nm. After the annealing process, new small Cu particles appeared in the space between the as deposited ones, and all the particles were distributed more homogenously within the films. The resistivity of the DLC films decreased first with the addition of copper from 10 Ω·cm to 6×10^{3} Ω·cm, and secondly with the annealing process from 4×10^{-2} Ω·cm to 3 Ω·cm. Raman spectra show the tendency of the DLC films to become more graphitic with increasing annealing temperature, which may be one possible contribution to increased conductivity of the annealed Cu-DLC films.

Acknowledgement

The authors would like to thank Mr. Král for technical assistance. This work was done in Center of Excellence CENAMOST (Slovak Research and Development Agency Contract No. VVCE-0049-07) and was financially supported by grants APVV-0628-06, APVV-0548-07, LPP-0149-09, DAAD 507 552 00 and VEGA 1/1103/11, 1/1102/11.

References:

[1] J. Robertson / Material science and engineering, R37, (2002) 129-281
[2] H.W. Choi et al. / Thin Solid Films 516 (2007) 248–251
[3] T. Ohno et al. / Diamond & Related Materials 20 (2011) 651–654
[4] A.T.T. Koh et al. / Diamond & Related Materials 19 (2010) 637–642
[5] Y.-H. Lin et al. / Thin Solid Films 518 (2009) 1503–1507
[6] K.I. Schiffmann et al. / Thin Solid Films 347 (1999) 60–71
[7] R. Koppert et al. / Solid State Sciences 11 (2009) 1797–1800
[8] M. Marton et al./ Vacuum 84 (2010) 65–7

Joining and welding of dissimilar materials for energy applications

Jean Pierre Bergmann, Franziska Petzoldt, Rene Schürer

Ilmenau University of Technology, FG Fertigungstechnik, Neuhaus 1, 98693 Ilmenau, Germany

Abstract

Content of the talk will be the description of procedures in order to weld aluminum to copper via solid state welding. Welding of dissimilar materials in order to reach a high strength and durable joint is a reasonable and outstanding challenge for industrial and especially for automotive application. Nowadays wiring systems and electrical systems, as for example batteries, turn out to be main drivers for hybrid joints. Joining of aluminum to copper through a melting process leads to brittle intermetallics, which cause failure of the joint during cooling.

Solid state welding allows the welding below melting temperature, so that phenomena at the interface, which lead to formation of intermetallics under different conditions, are interesting for the resulting properties of the joints. Not only mechanical properties, but electrical resistivity and heat conduction are strongly dependent from it. Diffusion welding is performed as a model welding procedure, while friction stir welding and hybrid friction diffusion bonding are investigated as technological welding processes in this paper. Furthermore the long time properties of US-joints will be depicted.

Werkstoffentwicklungen für Brennstoffzellen

Prof. Dr. Oliver Schneider

TU München, Lehrstuhl für Technische Physik (E19), James-Franck-Str. 1, 85748 Garching, Germany; E-Mail: oliver_m.schneider@tum.de

Abstract

- neue Kathodenkatalysatoren für PEM-Brennstoffzellen

- neue Elektrolytmaterialien für High-Temperature PEM

- Modifikation von Anodenmaterialien in der Hochtemperatur-SOFC

- Aspekte der Direktkohlenstoffbrennstoffzelle.

Metallization Cost Reduction in c-Si PV: Inline Equipment and Processes for Copper Plating

Dr. Holger Kühnlein

R&D Manager Back End, RENA GmbH, Solar Technology Center Freiburg , Hans-Bunte-Strasse 19, 79108 Freiburg im Breisgau, Germany; holger.kuehnlein@rena.com

Abstract

The presentation shows the status of plating equipment and performance for the introduction of copper plating in PV. A short overview will give an impression on the challenges to start plating from Ag on Paste up to Ni/Cu/Ag on Si. A detailed cost discussion in respect to the required technical solutions for fine line print and laser ablation will show the roadmap via a Ag reduced to a complete Ag free solar cell.

Developments in Batteries and Energy Storage

Vikram Godbole

Robert Bosch Battery Solutions GmbH, RBDB/ENC, Postfach 300220, 70442 Stuttgart, Germany

Abstract

With the advent of renewable energy as a viable replacement for the fossil fuels, energy storage has become an important topic. There exist many energy storage systems, of which the electrochemical energy storage systems viz. batteries, are gaining more and more attention. Batteries, based on Li-ion technology, are widely used in consumer electronics like cell phones, laptops, etc. and have considerable potential for use in the electromobility sector. A short overview of the currently available electrochemical energy storage systems will be given with focus on development in the Li-ion battery field. Main breakthroughs and challenges of Li-ion batteries will be discussed and the activities of Robert Bosch GmbH in the field of electromobility will be presented

Carbon-based Nanomaterials - Properties, Perspectives and Applications

Martin Hulman

International Laser Centre, Ilkovičova 3, 84104 Bratislava;
Danubia NanoTech s.r.o., Ilkovičova 3, 84104 Bratislava
Faculty of Electrical Engineering and Information Technology, Slovak Technical University, Ilkovičova 3, 84104 Bratislava

Abstract

Carbon nanomaterials, nanotubes and graphene, have evolved from objects of a pure scientific interest to materials with an extremely high technological potential. Their exceptional physical properties have made them superior in many aspects to materials used so far for some particular applications.

Graphene is a single-atom thin sheet of carbon atoms and a carbon nanotube is a rolled-up sheet of graphene. From a structural point of view, they can be considered as materials having only the surface and no interior. This fact makes both nanomaterials highly susceptible to any environmental influence. Owing to their high electrical and thermal conductivity and electron mobility, carbon nanotubes and graphene can transmit perturbations very rapidly and with a high efficiency.

Among the most exploited properties of carbon nanomaterials is their high surface to volume or surface to weight ratio. They are also mechanically very robust and stable. High surface to volume ratio in combination with excellent electrical properties make carbon materials very promising candidates for applications focused on conversion and storage of (electrical) energy.

In my talk, I will briefly introduce physical properties of graphene and carbon nanotubes and then proceed discussing some applications related to the energy conversion and storage. Among the applications, I will mention solar cells, ultracapacitors, fuel cells and some other. Comparison of the latter with the state-of-the-art products will conclude the talk.

Metal-insulator nanostructured films for magnetoelectronic devices: properties and applications

J. Fedotova[1], J. Kasiuk[1], J Przewoznik[2], Cz Kapusta[2], M.Milosavljević[3], T. N. Koltunowicz [4], P.Zhukowski[4], I.Svito[5], V.Baev[1], A.Maximenko[1]

[1] Belarusian State University – NC PHEP, M.Bogdanovich Str.153, 220040 Minsk
[2] AGH University of Science and Technology, Faculty of Physics and Applied Computer Science, Department of Solid State Physics, 30-059 Krakow
[3] VINČA Institute of Nuclear Sciences, Belgrade University, P.O. Box 522, 11001 Belgrade, Serbia
[4] Lublin University of Technology, Nadbystrzycka Str. 38a, 20-618 Lublin
[5] Belarusian State University, Nezavisimostci av. 4, 220030 Minsk

Abstract

Progress in designing of new magnetoelectronic nanostructures, particularly, for exploitation at frequencies up to GHz requires new artificial materials combining tunable magnetic and electric properties with low-cost technological opportunity to form miniature devices. Recent experiments have proved that in this context metal-insulator film heterostructures are prospective for synthesis of materials with tailored physical properties that could be controlled with external magnetic and electric fields.

Summary of recent experimental results on phase composition, magnetic properties, magnetoresistivity and electrical conductivity of nanostructured composite thin films including multiferroic and thermoelectric films for high-frequency applications is presented. Technological approaches based on variation of their chemical and phase composition and deposition regimes are proposed for tuning films properties towards their desired combination with respect to potential application in designing of planar (non-coil) inductive elements, thermoelectric microgenerators, magnetic sensors, etc. Physical mechanisms and models responsible for magnetic and electric properties of composite films are analyzed.

Additionally, structure and properties of functional template-assisted composite/multilayered nanostructures on semiconductive substrate with controlled shape and composition for preparation of tunable magnetoelectronic devices are discussed. Effect of magnetoresistivity modulation realized on Schottky metal/semiconductor barrier by application of external voltage to template-based nanostructures is considered.

1 INTRODUCTION

Modern trends in the designing and analysis of new materials for magnetoelectronic devices (transducers, sensors, electromagnets) generally reflect the increasing demand for multifunctional fine scale integrated systems demonstrating peculiar combination of tuneable magnetic and electronic properties, compatibility with silicon processing planar technology and low production costs [1,2]. Basing requirements for such materials, particularly, operating at frequencies up to GHz range include high saturation magnetization M_S, and electrical resistivity ρ combined with high permeability μ in MHz-GHz band and low coercive force H_C. Metal-insulator (*M-I*) magnetic nanostructured films (Fe,Co,Ni-SiO_2, Al_2O_3, CaF_2, ZrO_2, $PbZrTiO_3$) where local phase and/or structural inhomogenities, enhanced surface contribution and quantum electronic and magnetic effects draw to distinct deviation of functional properties as compared to their bulk counterparts fully satisfy abovementioned requirements. *M-I* film heterostructures sintered with ion-beam sputtering technique possess M_S up to 1800

κA/m, H_C less that 4 kA/m (at RT), μ up to 200 at 50 MHz and ρ ranged between 10^{-2} and10 Ohm·m. An alternative technological approach for designing nanocomposite materials with tailored properties is fabrication of TEmplate-assisted COmposite *M-I* NAnostructures on Semiconductive Substrate (TECONASS nanoarrays).

Present article is therefore focused on some recent scientific and technological results in ion-beam and template-assisted processing of *M-I* magnetic nanostructured films and their application in designing of planar (non-coil) inductive elements, thermoelectric microgenerators and microrefrigerators, magnetic sensors, etc.

2 EXPERIMENTAL DETAILS

$(FeCo)_x(I)_{100-x}$ ($31 \leq x \leq 81$ at. %) nanocomposite films (1 to 6 μm) where *I*=Al_2O_3, CaF_2, $PbZrTiO_3$ were sintered by ion-beam sputtering of complex target (containing *I* strips on *M* substrate) in oxygen-free and oxygen-containing sputtering ambient onto glass-ceramic and Al substrates. TECONASS nanostructures were prepared by electrochemical deposition of Ni and Co inside anodic Al_2O_3 template or porous SiO_2 template fabricated by nuclear ion track etch method on Si and GaAs substrates.

Composition of nanostructures was verified by TEM and HRTEM (Philips EM400T and Philips CM200), XRD (Empyrean PANalytical diffractometer, Cu K_α radiation), EXAFS-XANES (beam line ID26 of the European Synchrotron Radiation Facility) and Mössbauer spectroscopy in the temperature range T = 77 – 300 K. Magnetic properties of films were studied by *Quantum Design VSM-PPMS* in the range of T = 2 – 300 K in magnetic fields H up to 89 kOe. DC/AC resistivity and magnetoresistivity *MR* of samples were measured by four-probe method (Cryogenics Ltd closed-cycle refrigerator system) at T = 2– 300 K in magnetic fields H up to 80 kOe.

3 RESULTS AND DISCUSSION

3.1 Ion-beam assisted FeCo-Al_2O_3, CaF_2, $PbZrTiO_3$ films

$(FeCo)_x(Al_2O_3)_{100-x}$ sputtered in atmosphere with added oxygen contain nanogranules with “metallic core-oxide shell” structure (see Fig 1). Formation of such a structure composed of crystalline metallic *bcc* α-FeCo-based nanosized cores encapsulated in an amorphous oxide shell, all embedded in the amorphous Al_2O_3 matrix, is revealed with TEM and HRTEM. EXAFS and XANES exhibit selective oxidation of nanoparticles – almost full oxidation of iron, while cobalt is found to be oxidized only partially. In strong correlation with the Mössbauer spectroscopy as well as with the results of electron- and X-ray diffraction it shows that for $x \leq 56$ the metallic core constitutes *bcc* FeCo solid solution, possibly enriched with Co, while oxide shell mainly consists of mixed Fe-rich oxide.

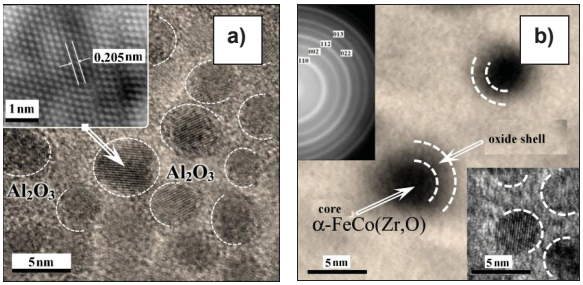

Fig 1: HRTEM (a) and TEM (b) for FeCo-Al_2O_3 film sintered in oxygen-containing atmosphere

Oxidized films reveal VRH (tunneling) conductivity in accordance with Mott's or Shklovski-Efros laws dominating for different *x,* and metallic conductive cluster network is not formed. This should be related to the formation of oxide shells preventing coalescence of metallic nanogranules with increasing metallic contribution in films.

Negative *MR* of spin-dependent nature is observed for oxidized granular films in the whole range of *x* values (see Fig 2). Enhanced negative *MR* effect in the films with the "core-shell" structure within $x = 55$ is assigned to the stabilization of the metallic cores sizes within optimal (single-domain) size owing to encapsulation inside oxide shells as well as to spin accumulation and spin filtering processes [3]. Oxidized films possessing M_S up to 695 kA/m, H_C less than 0,02 kA/m and ρ ranged between 4,6-540 мОм·м are very good high-frequency magnetically soft material [4].

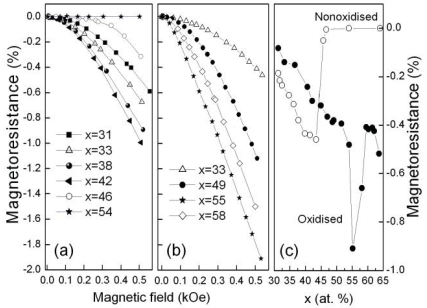

Fig 2: *MR(H)* curves for non-oxidized (a) and oxidized (b) FeCo-Al_2O_3 films. *MR*(x) for FeCo-Al_2O_3 films (c)

Oxidized $(FeCo)_x(Al_2O_3)_{100-x}$ subjected to annealing (at ≈ 880 K) reveal positive values of the phase angle shift θ (see Fig 3a) interpreted as a negative capacitance effect corresponding to inductive contribution to real part of admittance. The value of "effective" inductive contribution *L* was estimated to be as high as 20 $\mu H/\mu m^3$ at 1 MHz basing on the correspondent equivalent circuit (see Fig 3b) that is much higher than in the case of known diods, p-n-p junctions, metal-semiconductor interfaces. Observation of the inductive contribution is prospective for designing of planar

noncoil-like inductances for high-frequency applications compatible with silicon planar technology [5].

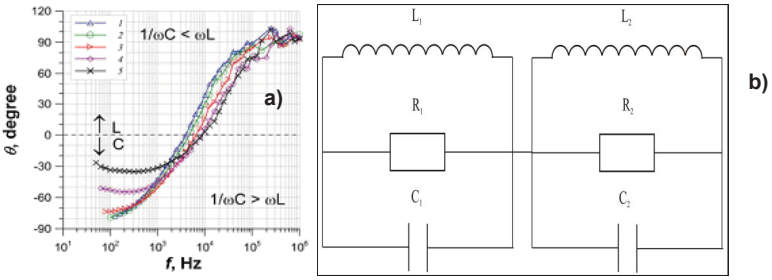

Fig 3: Typical $\theta(f)$ curves for the as-deposited FeCo-Al_2O_3 films sintered in oxygen-containing atmosphere at measured at T = 153 K (1), 178 K (2), 218 K (3), 258 K (4), 293 (5) (a) and correspondent equivalent circuit (b)

Desired stabilization of granular nanostructure in multiferroic $(FeCo)_x(PbZrTiO_3)_{100-x}$ films for $x \leq 53$ at.% sintered in oxygen-containing atmosphere due to selective oxidation of nanoparticles and stabilizing role of oxide shells is experimentally proved by XRD, EXAFS and Mössbauer spectroscopies, magnetometry and resistivity measurements. For $\theta(f)$ dependencies of $FeCo\text{-}PbZrTiO_3$ films (see Fig 4a) reveal inductive-like behavior at 303 K when f > 3 kHz even without post-synthesis annealing. Basing on the interpretation of $\theta(f)$ curves with the equivalent circuits the L value was estimated to be as high as 20 μH/μm^3 at 1 MHz.

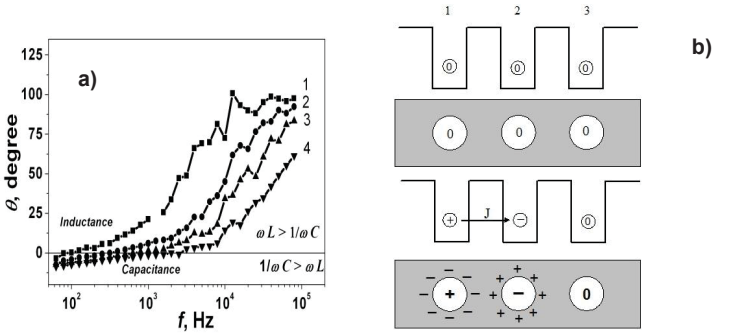

Fig 4: Typical $\theta(f)$ curves (a) for the as-deposited FeCo-$PbZrTiO_3$ films sintered in oxygen-containing atmosphere at measured at T = 243 K (1), 263 K (2), 283 K (3), 303 K (4). Model for AC/DC conductivity inducing the formation of noncoil-like inductive contribution in *M-I* films (b)

Observed “effective” inductive contribution in granular films were interpreted within the frame of the proposed model of AC/DC hopping conductance of electrons over selectively oxidized nanoparticles embedded into Al_2O_3 and $PbZrTiO_3$ matrixes. Its scheme is shown in Fig 4b. Positive phase shift angle of the applied voltage against the electric current is related to the formation of dipole – positively and negatively charged nanoparticles – due to the first jump of electron to the neighboring nanoparticle (potential well). Polarization of dielectric matrix surrounding nanoparticles due to the formed dipole is the origin of the increased electron mean life time in a potential well (nanoparticles) delaying its next jump. Such a time delay resulted in the electric current shift with respect to the applied voltage.

3.2. TECONASS nanostructures

Recently, experimental study of *Si/SiO₂/Ni* nanoarrays (see structure in Fig 5a) prepared in the form of Schottky barriers revealed giant *MR* effect. As is seen from Fig 5b, application of magnetic field both normally and along surface of *n-Si/SiO₂/Ni* nanostructures resulted in increase of electrical resistance. This is evident from the change of I-V characteristics slope defining the *R* value. As shown in Fig. 5c, the *MR* values were maximal at the temperature of 25 K and dependent on electric current reaching magnitudes of 200 – 500 % at the maximum point.

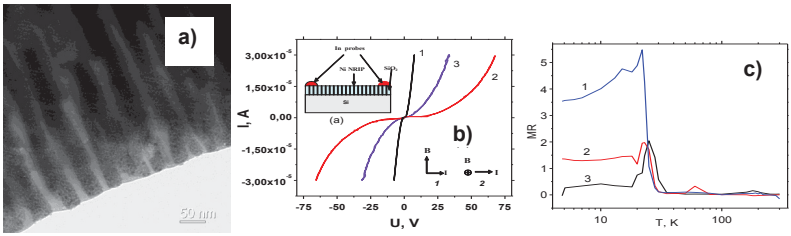

Fig 5: TEM image of n-Si/SiO_2/Ni structure (a). *I-U* characteristics of n-Si/SiO_2/Ni structure at 25 K for zero magnetic field *H* (1), *H*= 8 T directed normally (2) or along (3) sample surface (b) and *MR* temperature dependences for different electric current *I* values (c) *I* = 10 nA (1), 100 nA (2) and 1000 nA (3)

Very similar effect was obtained on double-layer structure *SiO_2(Co)/GaAs* at *RT*. Present experiments presumes that desired high *GMR* effect could be achieved at room temperature when Si substrate will be substituted with GaAs that is more prospective for application in industry. Basing on these preliminary results one can assume that deposition of ordered nanoarrays set onto semiconductive substrate (Si, GaAs, etc.) with the additional back-side electrode open the opportunity to form the network of MOS-like electronic element modulating (enhancing or suppressing) their *MR* effect. Every nanoarray should be considered as a separate MOS-like electronic element.

4 CONCLUSIONS

M-I multifunctional film heterostructures with tunable magnetic and electric properties sintered with ion-beam sputtering technique or template-assisted electrodeposition are proved to be very promising for designing the variety of new magnetoelectronic devices. Particularly, *M-I* magnetic and multiferroic films with enhanced *MR* effect as well as negative capacitance effect (up to 20 $\mu H/\mu m^3$) related to the selective nanoparticles oxidation and formation of "core-shell" nanostructure could be applied for high-frequency planar magnetic sensors and noncoil-like inductances. Versatile intrinsic properties of TECONASS *M-I* nanostructures revealing tunable *GMR* effect could be successfully utilized in transistors, microelectrodes, diodes, moulds for MEMs. The important advantages of the proposed heterostructures are their compatibility with silicon planar technology, low production costs as well as reliable and well reproducible technology processing.

Acknowledgements

We acknowledge ESRF for the provision of beam time and thank the ID26 staff for help in setting up the experiment. We also acknowledge the support from the Belarusian State program "Functional materials", project 1.16, the Polish Ministry of Science and Higher Education, the Serbian Ministry of Sciences and Technological Development, project OI 171023, EU COST Action MP0903 Nanoalloys, and EU FP7 SILAPMS project 226470.

References

[1] M. E. McHenry et al. Amorphous and nanocrystalline materials for applications as soft magnets, Progr. Mater. Sci. **44** (1999) 291–433.

[2] F. Mazaleyrat, L.K. Varga. Ferromagnetic nanocomposites, J. Magn. Magn. Mater. **215-216** (2000) 253–259.

[3] J. Fedotova, J. Przewoznik, Cz. Kapusta, M.Milosavljevic, J.V. Kasiuk, et al Magnetoresistance in FeCoZr-Al_2O_3 nanocomposite films containing "metal core-oxide shell" nanogranules, J. Phys. D: Appl. Phys. **44** (2011) 495001-1.

[4] J. Fedotova, J. Kasiuk, J. Przewoznik, Cz. Kapusta et al. Effect of oxide shells on the magnetic and megnetotransport characteristics of oxidized FeCoZr nanogranules in Al_2O_3, J. Alloys Compd **509** (2011) 9869-9875.

[5] P.Zhukowski, T.N.Koltunowicz, A.Fedotov, J.Fedotova, A.Larkin. A method for fabrication of noncoil-like inductivities for microelectronic systems, Patent 22.09.2011, Biuletyn urzedu patentowego Rzeczypospolitej Polskiej **20** (2011) 35.